TOWARD IMPROVED CONSTRAINTS ON METHANE EMISSIONS FROM OIL AND NATURAL GAS FIELDS

by

Lacey Holland

A dissertation submitted to the faculty of
The University of Utah
in partial fulfillment of the requirements for the degree of

Doctor of Philosophy

Department of Atmospheric Sciences

The University of Utah

May 2018

The University of Utah Graduate School

STATEMENT OF DISSERTATION APPROVAL

The dissertation of **Lacey Holland**

has been approved by the following supervisory committee members:

John Chun-Han Lin	, Chair	**12/9/2016** Date Approved
Kevin D. Perry	, Member	**12/9/2016** Date Approved
Gerald G. Mace	, Member	**12/9/2016** Date Approved
James R. Ehleringer	, Member	**12/9/2016** Date Approved
Charles Miller	, Member	Date Approved

and by **Kevin D. Perry**, Chair/Dean of

the Department/College/School of **Atmospheric Sciences**

and by David B. Kieda, Dean of The Graduate School.

ABSTRACT

Methane, the primary component of natural gas, is a potent greenhouse gas with 28-34 times the global warming potential of carbon dioxide on a 100-year timescale. Although natural gas is touted as a bridge fuel, one study suggests no climate benefit to the use of natural gas over coal as an energy source if fugitive emissions (emissions lost to the atmosphere) exceed 2% of production. To assess the climate impact of natural gas production, emission estimates are needed to detect and monitor fugitive emission rates. In some gas fields within the U.S., such as the Uinta Basin, as much as 12% of natural gas production may be lost as fugitive emissions.

I will present the Lagrangian Estimation of Aircraft-derived Fluxes (LEAF) method to estimate methane emissions over the Uinta Basin. This technique combines a novel time series with the Stochastic Time-Inverted Lagrangian Transport (STILT) model to develop a flexible framework with fewer meteorological requirements for validity than other commonly used methods.

TABLE OF CONTENTS

LIST OF FIGURES

Figures

ACKNOWLEDGMENTS

I would like to express my sincerest gratitude to all of those who provided help, encouragement and support as I pursued my graduate degree. Among those are Kenneth and Paula Holland, Dixie Holland, Tammy Whetsell, Stephannie Holland, Kenndra Anthony, John Gleason, Raili Taylor, Clive Taylor, Bhavani Rajan, Carl Etsitty, Preston Heard, and many others. I could not have done this without your help and my appreciation is forever yours.

CHAPTER 1

INTRODUCTION

In atmospheric transport and dispersion models and atmospheric inverse studies, the Planetary Boundary Layer (PBL) height is an important parameter to simulate chemical concentrations. Emissions from within the PBL are largely well-mixed and confined within it. Air quality forecast models and simulations have a high degree of sensitivity to uncertainties in the PBL height (Kretschmer et al. 2012; Lin et al. 2006), and an improved understanding of these uncertainties has been shown to improve simulations of trace gases (Kretschmer et al. 2014).

During the day, surface latent and sensible heat fluxes drive the turbulent processes within the daytime PBL, or Convective Boundary Layer (CBL). Another important process that affects PBL heights is mechanical mixing, or mixing from the turbulence that wind shear generates. These processes as controls on PBL height development are explored in Chapter 2.

When one assumes a constant chemical emission rate over a given area of interest with no other influencing effects, the CBL has a strong influence on measured atmospheric concentrations near the surface. As the CBL develops, these concentrations are diluted as air from the free atmosphere with lower concentrations of the emitted chemicals is entrained into the CBL. PBL growth, then, is essential to understand and to

simulate chemical emissions within the atmosphere.

In reality, chemical emission rates may exhibit spatiotemporal variability. In addition to changes in the PBL height, other factors such as atmospheric transport also alter estimates of atmospheric emissions. However, the impact of atmospheric transport and other factors is understood more easily with improvements in the simulation of PBL heights. One example of the importance of PBL height growth on emission estimates is shown in Chapter 3, wherein methane emissions are estimated with the use of airborne measurements. Inaccurate initial PBL heights required a bias-correction to improve emission estimates over an oil and natural gas producing area, the Uintah Basin. This correction and the ability to account for the impact of atmospheric transport led to improvements in aircraft-based estimates of methane emissions from oil and natural gas extraction.

Presented within this dissertation are two topics, interconnected through improvements in the understanding and simulation of the PBL, that seek to further the current understanding of GHG emissions:

1. Global analyses of Planetary Boundary Layer (PBL) growth
2. Lagrangian experiments to quantify methane emissions with airborne observations in the Uinta Basin

These topics relate to each other in that a better understanding of the PBL and its growth improves current understanding of methane emissions and conclude in Chapter 4.

CHAPTER 2

HOW MUCH VARIABILITY IN DAYTIME PLANETARY BOUNDARY LAYER HEIGHT CAN BE EXPLAINED WITH SURFACE HEATING OVER AND TIME (SHOT) MECHANICAL MIXING AND SURFACE HEATING (MASH) MODELS?

2.1 **Introduction**

The planetary boundary layer (PBL) is the interface for interactions between the atmosphere and Earth's surface. Exchanges of mass and energy within the PBL are fundamental to weather, climate, and air quality (Stull 1988). These exchanges impact atmospheric phenomenon on timescales that span minutes to years, and on spatial scales that span the micro- to global scales. The numerous effects on both weather and climate include, but are not limited to, the following: cloud cover, convective initiation, local circulations, and global circulations (Denning et al. 1996; Garratt 1993; Garrett 1982; Pielke et al. 1998; Smith et al. 1992; Yan; Anthes 1988). The PBL height (PBLH) is also the vertical depth through which substances emitted from the surface (e.g., air pollutants and greenhouse gases (GHGs)) are mixed, diluted, and transported (Holzworth 1967). For this reason, PBLHs are of particular importance to air quality models, tracer transport models, and atmospheric inversion studies that estimate surface emissions from atmospheric concentrations (Gerbig et al. 2008; Kretschmer et al. 2012; Lin et al. 2006)

on both regional (Gerbig et al. 2009) and global scales (Denning et al. 1995).

Numerous studies necessarily rely on PBLH estimates from meteorological reanalyses or numerical weather prediction (NWP) models. Most reanalysis and NWP-based PBLH products are derived from, or depend upon, vertical profiles of atmospheric variables. The upper-air observations incorporated in reanalyses through data assimilation procedures are both infrequent and sparse, relative to surface-based observations. This implies that reanalysis-based PBLH estimates depend upon the broad spatial attribution of sparsely observed upper-air variables and simulated changes in these variables between infrequent observation times. These estimates are subject to large uncertainties and errors. For instance, one study showed that the ECMWF Reanalysis-Interim PBLH product displayed mean errors on the order of 200-1000 m during summer in the tropics when compared to estimates derived from rawinsondes (von Engeln; Teixeira 2013). Among existing reanalysis products, differences can exceed 750 m even in relatively data-rich regions such as the U.S. and Europe (McGrath-Spangler; Denning 2012; Seidel et al. 2012). We also find because urbanization affects 2-m temperature (Arnfield 2003), surface temperatures (Peng et al. 2011), and radiative properties (Ramanathan and Feng 2008) have been documented, there is also likely a link between urbanization and PBLH.

As an effort to help improve predictions of PBLH around the world, we ask a basic question: **How much variability in PBLH around the globe can the surface buoyancy flux and mechanically-generated turbulence explain?** This approach relates growth rates to the physical variables related to buoyancy- and mechanically-driven turbulence within and above the PBL, such as sensible and latent heat fluxes, friction velocity, atmospheric stability above the PBL. Previous modeling work has shown that

surface heating and lower tropospheric stability account for most of the global spatial variability in PBLH within a global climate model (Medeiros et al. 2005). Field campaign studies likewise show the surface buoyancy flux to be the primary driver of PBLH variation on the mesoscale (Boers et al. 1984; Desai et al. 2005), and it is also known that mechanical turbulence can be of equal or greater magnitude than the buoyancy term under certain conditions (Stull 1976). These studies were restricted to limited domains. We will examine in a global analysis how much variability in PBLH the surface heating and wind shear can explain. In addition, we will examine the impact of urbanization on PBL model performance.

The simple model of PBL growth investigated here was developed and modified in closely related equations over the course of several decades (Ball 1960; Batchvarova; Gryning 1991; Carson 1973; Deardorff 1972; Lilly 1968; Stull 1976; Tennekes 1973; Tennekes; Driedonks 1981) and incorporates the surface heating and shear to PBL growth based on energetics. Previous studies validated the model over idealized locations or for short durations (e.g., Barr and Betts 1997; Stull 1976). To evaluate PBL height models based on Surface Heating Over Time (SHOT) and Mechanical Mixing And Surface Heating (MASH), we compare PBLHs derived from these methods to rawinsonde-diagnosed PBLHs and two current state-of-the-science reanalysis products: the Climate Forecast System Reanalysis (CFSR) and the European Center for Medium-Range Weather Forecasting (ECMWF) Reanalysis-Interim (ERA-I). We emphasize that the objective of this work is not to suggest that SHOT or MASH would replace more complex models of PBLH, but rather to assess how much variability in PBLH can already be explained by the known processes of surface heating and shear within the

model, despite the simplicity. In addition, we examine the impact of urban areas on PBLH and PBL growth model performance.

2.2 **Data and Methods**

2.2.1 PBL growth model description

The following equation estimates the rate of growth of the PBLH, denoted z_i, that excludes gravity waves and viscous dissipation (Stull 1976):

$$\frac{\partial z_i}{\partial t} = (1 + 2A)\frac{\overline{(w\prime\theta_{v\prime})}_0}{\gamma_\theta z_i} + \frac{2B\, u_*^3}{\gamma_\theta \beta {z_i}^2} \quad (1)$$

In (1), A and B are unitless empirical constants; γ_θ is the lapse rate of virtual potential temperature (θ_v) within the free atmosphere, above the PBL, as a measure of stability; $\overline{(w'\theta_v')}_0$ is the surface buoyancy flux (also known as the kinematic vertical turbulent heat flux); u_* is the frictional velocity. In this prognostic equation (1), changes in z_i are related to terms on the right-hand side: surface heating (buoyancy-driven PBL growth) and mechanically produced turbulence, respectively. Buoyancy-driven growth is parameterized to include the effects of entrainment at the top of the PBL through the inclusion of the parameter, A. As an entrainment parameter, A represents an empirically estimated ratio of heat flux across the entrainment layer, $-\overline{(w'\theta_v')}_h$, to the turbulent heat flux across the surface layer, $\overline{(w'\theta_v')}_0$: i.e., $A = -\overline{(w'\theta_v')}_h / \overline{(w'\theta_v')}_0$. This study uses the constant, global value of A=0.2 (Stull 1976a; Barr and Betts (1997)).

The second term on the right hand side (RHS) in (1) represents PBL growth due to mechanically-generated turbulence from the effects of surface friction (u_*), and also includes the empirically-determined parameter, B, that is said to range between 0 to >10

(Carson 1973). In this study, SHOT is the formulation of PBL heights that results from only the first term on the right in (1), while MASH is based on the full equation.

2.2.2 Observations from rawinsondes

This study focuses on available rawinsondes, a dataset that covers numerous locations around the world and offers observations for an extended period of time, to derive PBLHs and to extract many of the variables needed to run the SHOT and MASH models. Although a number of other observational methods to derive PBLHs are available (Seibert et al. 2000), many use instrumentation that is available for few sites or for limited amounts of time. The lapse rate above the PBL and initial PBL heights were extracted from rawinsondes and included in both SHOT and MASH.

2.2.2.1 *The Bulk Richardson Number method.* We apply the Bulk Richardson Number (BRN) method and formulation described in Seidel et al. (2012) to rawinsondes from the National Climatic Data Center (NCDC) Integrated Global Rawinsonde Archive (IGRA; (Durre et al. 2006)). The BRN is calculated for each vertical level within a profile:

$$Ri_b(z) = \frac{g\, z\, (\theta_v - \theta_{v0})}{\theta_{v0}\,((\Delta u)^2 + (\Delta v)^2)} \qquad (2)$$

Subscripts of zero indicate surface levels (z=0). Wind shear is calculated from differences in u and v components of the wind vector, between the surface and altitude above ground (z). Beginning near the surface, each rawinsonde is scanned upward until a critical value of 0.25 is exceeded. A linear in pressure interpolation between the level that exceeded a BRN of 0.25 and the level below is diagnosed as the mixing height (z_i).

When using the BRN, the number of observations taken in the vertical during

each rawinsonde ascent has an impact on the quality of PBLHs derived. Seidel et al. (2012) found that a minimum of seven rawinsonde observations under 500 hPa is required to adequately resolve the PBLH, a threshold also used in this study. Diagnosed PBLHs that exceed 4000 m AGL are removed from consideration. Likewise, any near-surface levels (< 10 m) are removed from consideration as a candidate PBLH. The next section describes quality control measures taken to control for changes to rawinsonde vertical resolution over time.

2.2.2.2 *Rawinsonde quality control and vertical resolution*. Methods were taken to ensure further the quality of PBLHs detected from rawinsondes. These include quality checks on the number of rawinsondes available at each site and checks on the long-term consistency of PBLHs.

To ensure the PBLHs detected used in the analysis are representative of each site, each site must report more than 60 valid daytime rawinsondes available for the period 2000-2009. After the exclusion of sites with an excessive number of missing rawinsondes, a total of 619 global sites are examined for the 2000-2009 period.

We also examined the quality of observations over time for any rapid changes or inconsistencies during the 2000-2009 period. In particular, the number of vertical levels, and thus detectable PBLHs, displayed a break point or sudden change at many sites. This is a result of changes in rawinsonde technology and equipment. To address this change, we adopted a unique strategy with the goal to retain a temporally-consistent number of vertical rawinsonde levels at each site.

2.2.3 Meteorological reanalyses and surface heat fluxes

Although the lapse rates above the PBL and initial PBLH were extracted from each rawinsonde, surface buoyancy flux and friction velocities also were needed to run SHOT and MASH. Reanalyses were used to retrieve these parameters from the grid point nearest each rawinsonde site.

Likewise, the PBLH from each reanalysis grid cell was extracted to serve as a baseline of comparison and to provide context for the analysis of the SHOT model performance. Because rawinsondes were assimilated in each reanalysis, the PBLHs derived from rawinsondes are not independent from the reanalysis PBLH products. The reanalysis PBLHs represent a benchmark of skill.

Both the CFSR and the ECMWF reanalyses were used in this study. The CFSR (Saha et al. 2010) from NCEP is a global reanalysis product at T382 (~38 km) horizontal resolution gridded output for the period 1979-2009. Sensible and latent heat fluxes and the friction velocity were produced in hourly increments within the CFSR. The ECMWF produces a global atmospheric reanalysis dataset, the ERA-I (Dee et al. 2011), at 0.125˚x0.125˚ horizontal resolution and 60 vertical levels. The necessary parameters are available in 3-hourly intervals within the ERA-I product.

2.2.4 SHOT and MASH implementation details

The implementation of the SHOT and MASH models required both the conversion of reanalysis variables and the derivation of variables from rawinsonde observations. The application of rawinsonde and reanalysis datasets to both the SHOT and MASH models is summarized in Fig. 2.1, including the hourly integrations

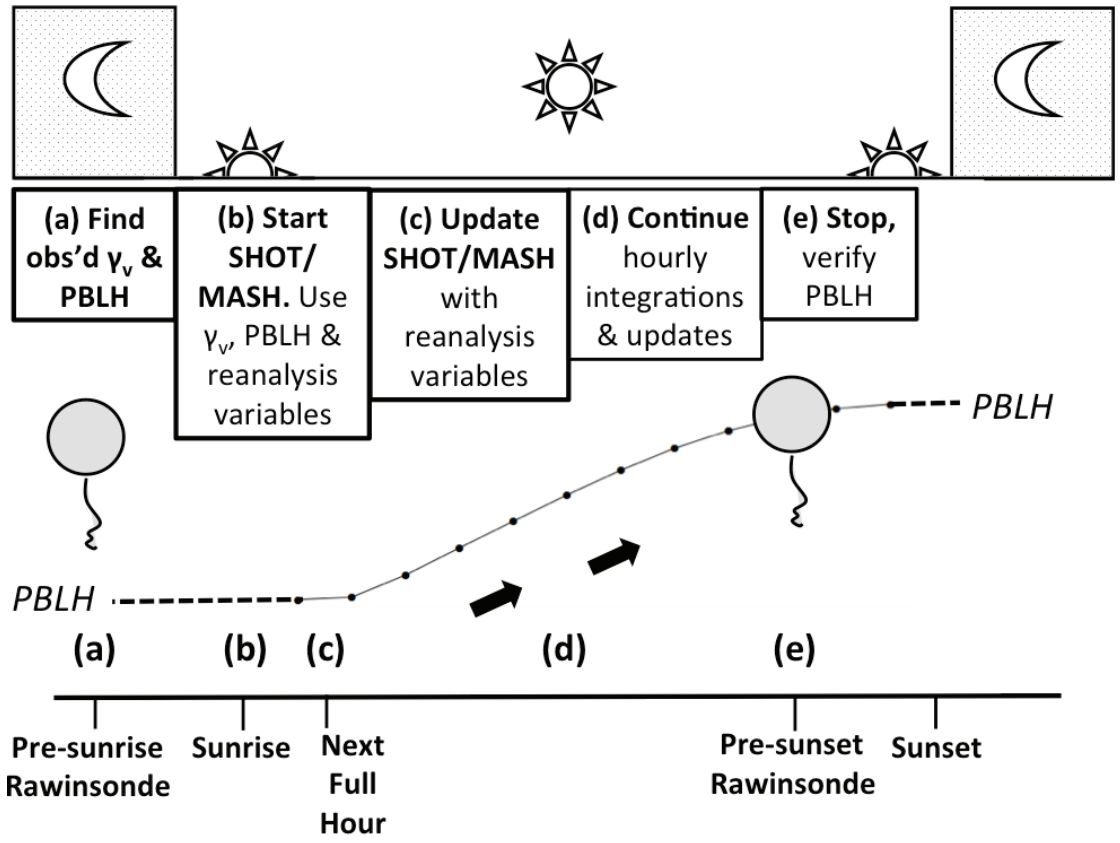

Figure 2.1: Overview of PBLH growth. As implemented in the SHOT/MASH models, PBL growth is depicted above in five stages: a) initialize with the PBLH (z_i) and virtual potential temperature lapse rate (γ_v) from a presunrise rawinsonde; b) integrate SHOT/MASH for fraction of hour between sunrise and the next full hour; c) begin hourly integrations with updates from reanalysis variables, d) continue integrations; e) final integration occurs in fraction of hour leading up to the last radiosonde launch before sunset. The dots connected with a black line indicate the simulated.

performed between sunrise and sunset.

Because both the surface buoyancy flux and the friction velocity are needed for hourly integrations of the SHOT and MASH models, each variable was either disaggregated or interpolated into hourly estimates and estimated for sunrise. Although the sensible heat flux contributes at least one order of magnitude more to the surface buoyancy flux, the latent heat flux was included for the sake of completeness.

The SHOT and MASH models were integrated beginning at local sunrise until the time of the daytime rawinsonde launch. Because sunrise often does not occur precisely at the beginning of a UTC hour, a smaller sunrise integration was used to simulate the fraction of hour between sunrise and the beginning of the next UTC hour. This integration included a corresponding fraction of surface buoyancy flux.

Launches that occur at night are excluded from the daytime PBL growth analysis and used only to determine the lapse rate in virtual potential temperature and an initial value for the PBLH. During the warm (cold) season of each respective hemisphere, both the 0000 UTC and 1200 UTC launch may both occur during daylight (nighttime) hours. In the case of two daytime rawinsondes, both soundings are retained, and the surface buoyancy flux is time-integrated over daylight and fractional daylight hours from local sunrise until the time of the last rawinsonde observation prior to sunset. The most recent prior nocturnal PBLH at that site is used to initialize each model for daytime PBL growth. The same is true of any missing rawinsonde-derived variable. There were six different models/reanalysis fields examined:

1. SHOT-C: Uses the NCEP CFSR reanalysis for surface buoyancy flux
2. SHOT-E: Same as SHOT-C, except for ERA-Interim reanalysis

3. MASH-C: Uses the NCEP CFSR reanalysis for the surface buoyancy flux and friction velocity
4. MASH-E: Same as MASH-C, except for ERA-Interim reanalysis
5. PBL-C: Reanalysis PBLH from CFSR reanalysis
6. PBL-E: Reanalysis PBLH from ERA-Interim reanalysis

Although we begin with examining the impact of reanalysis quality on each model, later only the ERA-Interim is examined and referred to as "MASH".

2.2.5 Rural/urban comparison

The Global Rural Urban Mapping Project (GRUMP; 2012) from the Center for International Earth Science Information Network (CIESIN) at the Earth Institute at Columbia University integrates census and satellite data to produce a grid of urban extents at 30 arc second resolution. GRUMP urban extents for the year 2000 is used to differentiate urban from rural areas at rawinsonde locations using the nearest GRUMP mask grid cell. The impact of urban and rural areas is examined.

2.3 **Results and Discussion**

SHOT and MASH are implemented for the 10 years including 2000-2009. We begin with an analysis of the performance impact reanalysis on the implementation of both the SHOT and MASH models. Then the overall and spatial distribution of mean monthly errors is examined. Finally, we examine the impact of urbanization on MASH performance.

2.3.1 Reanalysis impact

The effects of differences in the reanalyses (ERA-Interim and CFSR) on SHOT and MASH simulations are compared to reanalysis-produced PBLHs as performance benchmarks. The formulation of each model (SHOT vs. MASH) is also examined. All daytime 0000 UTC and 1200 UTC rawinsonde launches are used to make this comparison.

Although each model version uses the same rawinsonde-derived variables to initialize each model, the reanalysis selection has a large impact on SHOT and MASH performance. Figure 2.2 shows a Taylor diagram (Taylor 2001) that summarizes the performance of four models and two benchmark reanalyses. Taylor diagrams are polar plots that display measures of correlation (angle), standard deviation (radius), and centered Root Mean Squared Error (RMSE). In this diagram, a perfect model would have a correlation equal to one and a standard deviation equal to one radius. This area is denoted as an open circle on the bottom of the diagram. The distance from each model or benchmark to the perfect model is a gauge for the relative performance of each model.

We find the benchmarks (PBLH-C and PBLH-E) perform the best, while one of the models (MASH-E) approaches the same skill. Between the two benchmarks, the CFSR reanalysis PBLH (PBLH-C) shows a higher correlation than the ERA-Interim reanalysis PBLH (PBLH-E). MASH-E, the growth simulation that includes the ERA-Interim and the effects of mechanically-generated turbulence on PBL growth, has a correlation comparable to the benchmarks and a realistic standard deviation similar to that of the rawinsonde-based observations. The SHOT-C simulations vary too much and have the lowest correlation with observations (~0.5).

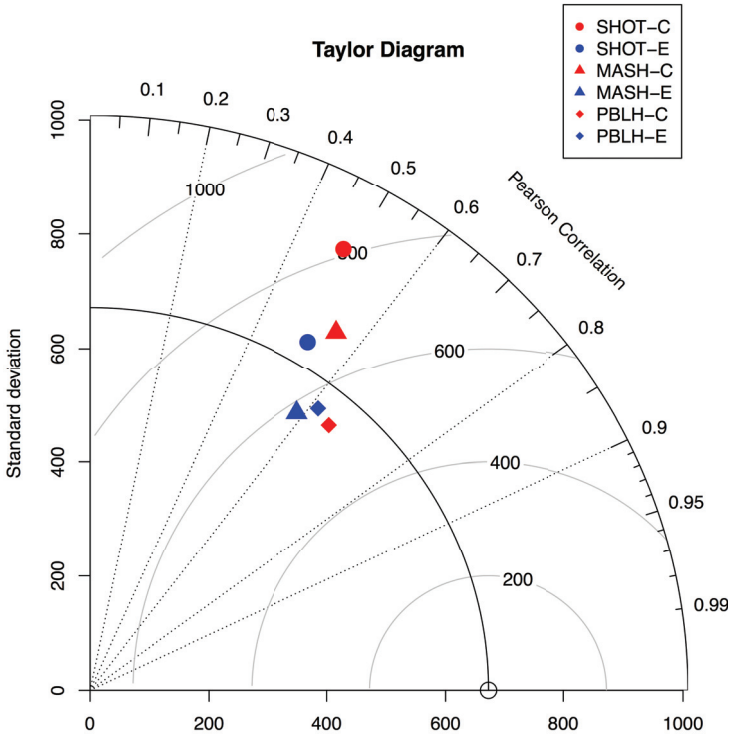

Figure 2.2: Taylor diagram showing global model performance for all rawinsonde locations and daily daytime launch times. The observed standard deviation is shown as an open circle with solid dark line. SHOT (circles), MASH (triangles) and the reanalysis PBL (PBLH; diamonds) are shown for the CFSR (red) and the ERA-Interim (blue).

The impact of the reanalysis seems to modify the variance, as gauged by proximity to the observed standard deviation (~650 m). The use of the surface buoyancy flux and friction velocity from the ERA-Interim lead to a realistically-varying PBLH in the MASH-E and SHOT-E simulations, while the use of the CFSR reanalysis (MASH-C, SHOT-C) produces simulations that vary too much.

The selection of MASH or SHOT model seems to impact the correlation the most. The inclusion of mechanically-generated turbulence increases the correlation with the observed PBLHs, in general, meaning large or small PBLHs correspond the most closely to like variations in the rawinsonde PBLHs.

While the choice of reanalysis has large impacts on the simulations, we also find the inclusion of more terms reduces the magnitudes of errors while increasing the correlation with observations. The use of the ERA-Interim with the MASH model leads to model skill that approaches that of the reanalysis PBLH benchmarks.

2.3.2 SHOT and MASH comparison to rawinsonde PBLHs

SHOT and MASH are two closely related models, with the MASH simulations including one term more than SHOT. However, the inclusion of more terms may not necessarily indicate the accurate simulation of the PBLH on longer-term means. Monthly means for the MASH and SHOT models based on the ERA-Interim reanalyses are compared to monthly-averaged observed PBLHs.

The magnitude of monthly means for each simulation is compared to rawinsonde PBLHs using the bivariate histogram in Fig. 2.3. The slope of the best-fit regression line and coefficient of determination are also shown.

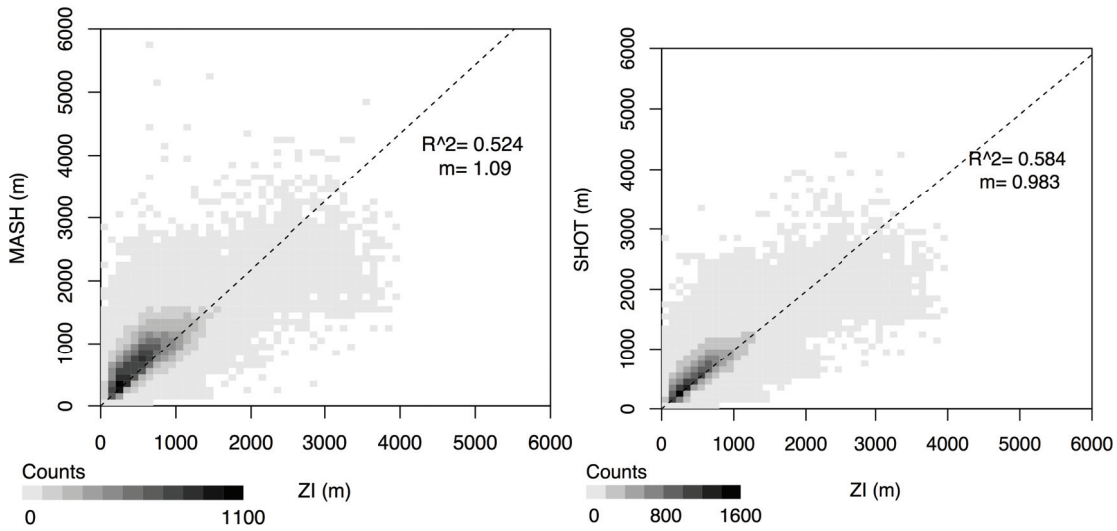

Figure 2.3: Bivariate histograms for the ERA-Interim based MASH model (left) and ERA-Interim based SHOT model (right) initializations showing the distribution of monthly averaged rawinsonde-derived PBLHs with simulated PBL heights for both 0000 UTC and 1200 UTC combined. The 1:1 line is shown as a dashed line. The coefficient of determination (R^2) is shown with the slope (m) of the least squares fit regression line (not shown).

On monthly time scales, the MASH and SHOT models perform similarly. Both exhibit very little forecast bias. The MASH model may have a slight tendency to grow too much, as evidenced by the greater than one slope. Surprisingly, on monthly time scales, the SHOT model performs slightly better than the MASH model. This may indicate that under day-to-day conditions, MASH is able to better characterize the variations in PBLH. However, when averaged into longer-term means, the SHOT may be better at characterizing the month-to-month differences.

2.3.3 Spatial comparisons of MASH performance

To investigate the potential use of the MASH model as a forecasting tool and to provide information about areas and time of day when SHOT model errors are the largest, daily correlation values are examined spatially.

Maps display the correlations between rawinsonde PBLHs and MASH at each site for 0000 UTC and 1200 UTC (Fig. 2.4) to show the relationship between performance and rawinsonde site location. For simulations valid at 00 UTC, the lowest correlations are generally found over western Asia, while the highest are over western North America. For 12 UTC simulations, the lowest correlations are found over the eastern U.S. and west of the International Dateline, while higher correlations are found over Europe.

For both 00 and 12 UTC, the lowest correlations are found on the western side of the daylit areas (western Asia and eastern U.S., respectively). Higher correlations are generally found on the eastern half of each area shown (western U.S., Europe). This may be related to stage of PBLH growth, with the earlier stages (western side) exhibiting the

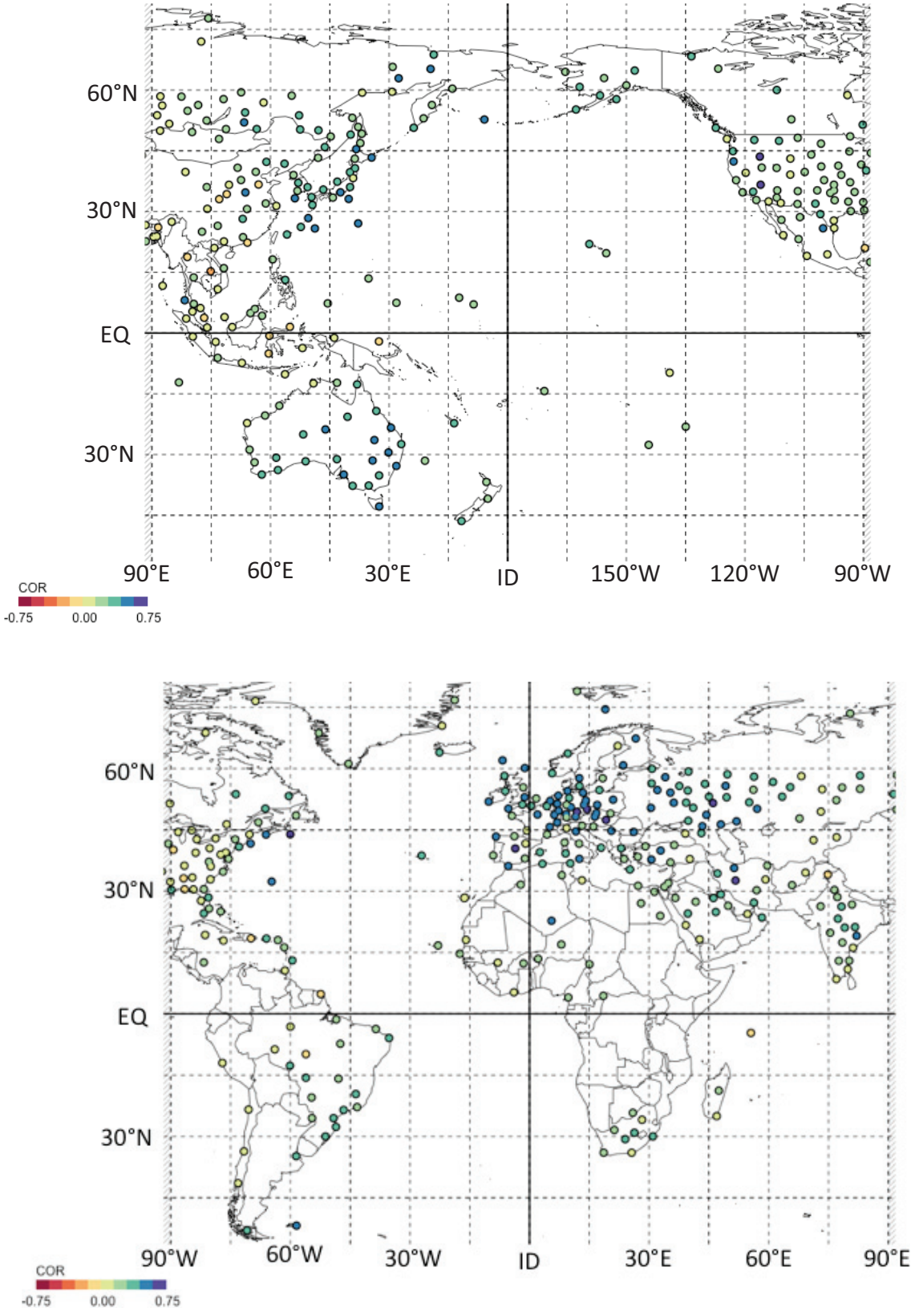

Figure 2.4: Pearson correlations for MASH-E for (a) 00 UTC and (b) 12 UTC.

largest errors.

2.3.4 A comparison of performance over urban and rural areas

Because of the known and demonstrated impact urbanization on relevant meteorological variables such as surface and skin temperatures, we include an analysis that shows the impact of urbanization on PBLHs. A global urban/rural mask was applied to each rawinsonde site. Daily PBLHs determined from rawinsondes and those simulated with MASH-E are shown according to sites that are broadly categorized as rural or urban.

MASH-E simulates too broad a range of PBLHs (Fig. 2.5), relative to observed in both urban and rural areas. The range is broader over rural areas than urban areas using the MASH model. For both the MASH and observed PBLHs, the rural sites demonstrate slightly higher PBLHs than the urban sites. Although increased surface temperatures may increase the surface buoyancy flux, other processes impact PBLH growth in these areas and warrant further exploration.

2.4 **Summary**

In this study, we explored the feasibility of an extremely simple model for simulating PBL growth, based on Surface Heating Over Time (SHOT) and Mechanical mixing And Surface Heating (MASH). Monthly and daily performance has been demonstrated through the global analysis of SHOT and MASH PBLHs based on both the ERA-Interim and CFSR reanalyses. These were compared to rawinsondes and reanalysis PBLHs. In general, the use of the ERA-Interim reanalysis products increased the skill of both the MASH and SHOT models. The longitudes associated with early stage PBL growth demonstrate the largest errors in the MASH model, while sites located in the

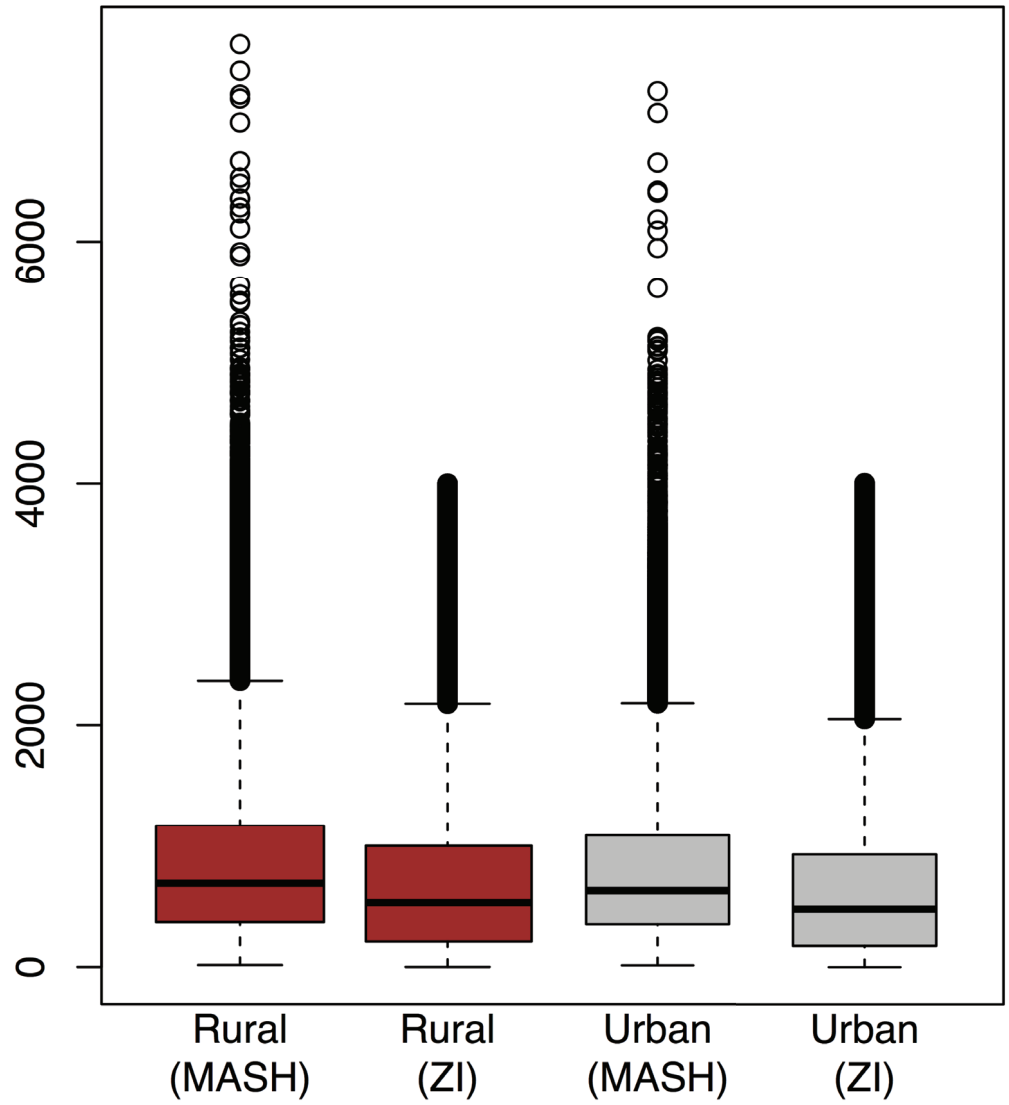

Figure 2.5: A global comparison of PBLHs (ZI) and the MASH model for rural (brown) and urban (gray) rawinsonde sites.

middle or eastern side of the area of interest (late growth stage) demonstrate smaller errors, with the exception of the areas at 12 UTC that are just to the west of the international dateline.

As implemented in this study, the SHOT and MASH models, despite their simplicity, are able to account for 52-58% of the monthly variance in observed PBLHs. This differs from, but approaches the lower bound of the 60-90% of variance explained in prior studies that explored the PBL growth model under clear-sky conditions until the maximum PBLH was reached (Boers et al. 1984; Desai et al. 2005; Medeiros et al. 2005; Stull 1976). We note also that this analysis did not exclude cloudy cases, which likely impacts model performance. Closely related PBL growth models that simulate other PBL processes may provide additional opportunities for further skill improvement in PBLH simulations.

Further development could result potentially in a stand-alone forecast tool that incorporates real-time meteorological observations with applicability toward air quality and other forecasts that rely on PBLHs. To further investigate the accuracy of the MASH and SHOT models, independent observations (i.e., observations unused in the reanalysis datasets) of the required parameters (e.g., surface buoyancy flux) globally would yield more conclusive evidence in a comparison against reanalysis-diagnosed PBLHs. Because rawinsondes were included in each reanalysis, the reanalysis PBLH products presented here served as an upper limit to predictability. A comparison against global forecast model-produced PBLHs would more conclusively demonstrate potential use in forecasting.

With only a limited number of parameters from a prior rawinsonde to initialize

MASH and SHOT, each shows potential as a stand-alone PBL height forecast tool that requires hourly surface heat fluxes and friction velocity. This study suggests that improvements to the MASH and SHOT models that alter or limit growth rates during the evening transition period may yield further skill improvements. These improvements are likely to be especially evident through the use of independent datasets. Overall, both are skillful models with the potential to reach the skill of current products and may be a viable alternative for climate and air quality applications.

CHAPTER 3

THE LAGRANGIAN ESTIMATION OF AIRCRAFT-DERIVED FLUXES (LEAF) METHOD OF METHANE FLUX ESTIMATION FROM OIL AND NATURAL GAS ACTIVITIES

3.1 **Introduction**

Methane is a potent greenhouse gas (GHG) with 28-34 times the global warming potential of carbon dioxide on a 100-year timescale (Shindell et al. 2009; Stocker et al. 2013). Furthermore, methane serves as a precursor that leads to production of ozone, which is both an air pollutant and GHG, making methane a global concern for air quality and climate. Relative to carbon dioxide (CO_2), reduction of methane emissions is also viewed as a more easily achieved climate goal (Montzka et al. 2011). For these reasons, the monitoring and assessment of atmospheric methane sources is important.

Globally, atmospheric methane concentrations have increased dramatically since the Industrial Revolution. Despite a period of virtually no trend from 1999-2006 (Dlugokencky et al. 1998), recent observations show renewed increases (Rigby et al. 2008). One study also suggested that most of the increase is from the U.S. (Turner et al. 2012). In general, the rate of increase is consistent with a 6 Tg/y (2000-2009) imbalance in the global methane budget (Saunois et al. 2016).

The global sources of methane include both biogenic and anthropogenic sources. Humans generally have limited direct control over biogenic sources of methane

emissions, some of which increase with increased global temperatures, such as permafrost melt (Delisle 2007) and wetlands sources (Bousquet et al. 2006). Large decreases in anthropogenic sources would ameliorate these increases.

Globally, major anthropogenic sources of atmospheric methane include fossil fuel production, agricultural activities, and landfills (Saunois et al. 2016). However, there is some disagreement about the current attribution of anthropogenic sources. Some recent studies have indicated that the increase in atmospheric methane concentrations derives from agricultural activity (Schaefer 2016), while others point to the fossil fuel industry (Schwietzke et al. 2016). One study also suggested that most of the global increase is from the U.S. (Turner et al. 2016). The correct attribution of anthropogenic methane sources is needed to decrease global atmospheric concentrations.

Of fossil fuel sources of methane, the largest source is natural gas production. The U.S. is now the largest producer of natural gas in the world (Doman 2016), and the primary component of natural gas is methane. Natural gas is often touted as a clean alternative to coal, and the speed with which natural gas powered plants are able to respond to demand is recognized as important to the integration of intermittent renewable energy sources such as wind (Energy 2010). For these and other reasons, natural gas plays an increasing role in our energy infrastructure. However, studies suggest climate benefits of natural gas are lost if fugitive emissions (emissions lost to the atmosphere) exceed 2% of production (Alvarez et al. 2012).

Within some natural gas-producing areas in the U.S., it may be important to monitor emissions over several years to assure the fugitive emission rate no longer exceeds the rate that enables climate benefits. One example is the Uinta Basin of Utah,

which is reported to have fugitive emission rates of 6-12% of production (Karion et al. 2013). The Uinta Basin is also not the only gas-producing area that currently exceeds this limit (Peischl et al. 2012; Pétron et al. 2014). The monitoring of emissions over the same region over successive years would confirm changes in emission rates over time. Methane emissions over the same region may change on a year-to-year basis as a result of changes in natural gas production rates, the impact of policy implementation, or even repairs or damages incurred through aging infrastructure.

Many view efforts to reduce fugitive emissions through infrastructure improvements as a positive for health, climate, and industry. With much to be gained in the reduction of fugitive methane emissions given limited resources, how do we strategically implement the much-needed infrastructure improvements?

We first need accurate estimates of atmospheric methane emissions on both regional and facility-level scales to resolve source apportionment issues and to enact and monitor mitigation policies. To that effect, federal and state agencies produce methane inventories, but most inventories underestimate emissions when compared to those derived from field observations (Karion et al. 2015). Independent estimates from field observations to assess the quality of publicly available inventories may also differ over the same region (Karion et al. 2015; Lyon et al. 2015). These estimates generally converge and fall within the bounds of uncertainty of each other over individual regions and when including multiple sampling days in the estimates.

Techniques to produce methane emission estimates can be broadly categorized as "top-down" (derived from atmospheric observations that are disaggregated) or "bottom-up" (relies on self-reports or inferences from surrogate processes that are combined to

produce a total).

Top-down techniques for regional estimates often use airborne platforms. The expansive areal coverage and access to regions that would be otherwise difficult to reach from ground-based mobile platforms make airborne measurements ideal for regional estimates. Airborne measurements also allow emissions to be estimated in places with few or no stationary concentration measurements, particularly in regions with more immediacy than the time required to set up and establish the ground-based instrumentation necessary to acquire an archive of measurements. However, the expenses associated with aircraft deployment often limit the number and length of flights.

Top-down techniques that maximize the number of flight opportunities also provide more opportunities to monitor methane emissions. One such technique is the "mass balance" approach, in which a box model is used to estimate emissions based on differences between the measured upwind and downwind concentration, often under assumptions of steady atmospheric flows. This makes estimates of errors due to wind variability and turbulent dispersion difficult to include in estimates using this method. Flux estimation techniques that are robust to changes in wind speed and direction can yield additional information about spatial variability. This is particularly important because many areas of natural gas development can be described as lying in complex terrain or in areas affected by mesoscale wind circulations. The mesoscale wind circulations observed in areas of complex terrain often have a time-varying component related to physical attributes of the surrounding topography (Zhong et al. 2004) and may limit the applicability of some top-down techniques.

One flexible top-down technique is the use of a Lagrangian Particle Dispersion

Model (LPDM). Wind-following airborne measurements fit well within a Lagrangian model framework and even allow for the potential quantification of temporally varying emissions. This study provides a much-needed look at LPDM-based techniques of flux estimation.

Lin et al. (2004) applied the Stochastic Time-Inverted Lagrangian Transport model (STILT), an LPDM used widely to estimate trace gas emissions because of its time reversibility, to airborne measurements to estimate carbon dioxide fluxes. Other studies have used FLEXPART with WRF to quantify methane emissions in the San Joaquin Valley (Gentner et al. 2014), but used aircraft measurements as validation of FLEXPART footprints that were developed based on ground measurements.

The goal of this study is to present an end-to-end top-down approach to estimate regional-scale methane emissions from aircraft measurements made over a natural gas field in the U.S. This approach leverages in situ aircraft observations from two field campaigns that took place over the Uinta Basin (Utah) during 2012-2013 to estimate methane emissions.

The Lagrangian Estimation of Aircraft-derived Fluxes (LEAF) begins with the framework described in Lin et al. (2004) and adds a proof of concept to define the STILT receptors used to estimate trace gas emissions from airborne measurements. Aside from the time-reversed trajectory forecasts that many systems lack, consistency between forecast and analysis allows the optimization of field campaign sampling strategies. LEAF also leverages a novel time series analysis method and a mesoscale meteorological analysis to produce regional-scale methane emission estimates that are both robust and versatile relative to techniques. The 3 February 2012 NOAA flights in the Uinta Basin for

which methane flux estimates were derived from Karion et al. (2013) served as a baseline for the evaluation.

3.2 **Methods**

The overall framework to estimate emissions with the use of aircraft measurements and a time-reversed LPDM is described along with the measurements and methods evaluated.

3.2.1 Framework

The approach described in this study leverages both existing LPDM tools and develops novel approaches (Fig. 3.1). Among the existing STILT tools are an LPDM-based aircraft forecasting planner to define air-following flight paths based on current NWP forecasts, a STILT-based wind validation tool to assess the quality of the simulations performed, and the STILT model itself. The more novel approaches involve the selection and definition of LPDM receptors and the method used to create an area-wide emission estimate based on methane fluxes estimated on the receptor level. These tools and methods differ greatly from the way emissions are estimated using stationary measurements.

Emission estimates made through the use of an LPDM applied to stationary concentration measurements differ greatly from estimates made using airborne measurements. A common way to estimate emissions with stationary measurements is to collect concentration measurements from a large number of wind directions over a lengthy period of time, then match to an emission grid, and perform a Bayesian inversion to yield

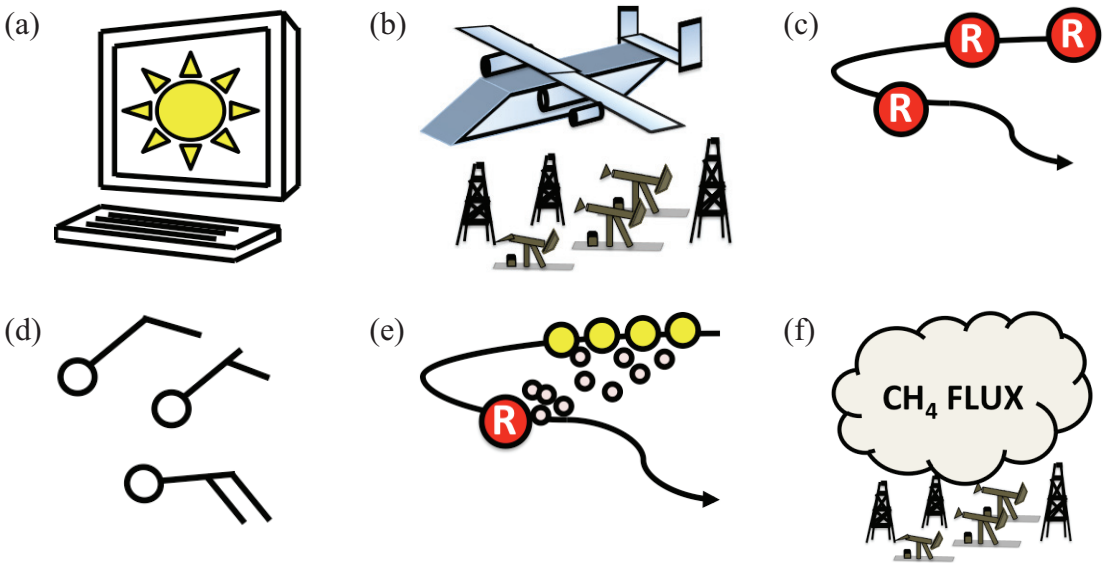

Figure 3.1: Overview of the LEAF system. When used end-to-end, LEAF begins with a forecast system (a) and ends with an emission estimate (f). After a forecast of the best place to sample emissions is made (a), measurements are collected (b). STILT receptors are defined based on change point methods applied to the relevant speciated concentration measurements (c). Receptor locations are used to create initial time-reversed STILT analyses (d), which are validated for any needed PBL height adjustments and to estimate wind error statistics and are used to create transport error runs. Matching between the time-inverted particles (e) and the upwind aircraft measurements is used to estimate emissions (f).

emission estimates over a broad area. This is difficult, if not impossible, to perform in areas with little or no history of concentration measurements.

The LEAF workflow (Fig. 3.1) is generally as follows:

- Forecasts made and used to create a flight plan
- Aircraft measurements are collected
- STILT receptors (i.e., where the model simulations are performed) are defined
- Assessment of analyses to be used (winds, boundary layer height)
- STILT simulations are performed
- Lastly, the estimation of fluxes and associated uncertainties.

The next sections describe the components of the workflow more thoroughly. These begin with the LPDM used in forecasts and flight planning, as well as to create the simulations necessary to estimate emissions and portions of the associated uncertainties.

3.2.2 The Stochastic Time-Inverted Lagrangian Transport model (STILT)

3.2.2.1 *Model description*. STILT is the primary tool used to create both real-time forecasts and the emission estimates. Back (time-reversed) trajectories are simulated from a location and initialization time – a receptor – that indicates where the air arrives and results in a change in measured concentrations. The back trajectories themselves indicate areas where the air parcels arriving at the receptor have been subject to surface influences, such as methane emission sources.

The back-trajectories represent the paths simulated particles take to arrive at the time and place of the STILT receptor – where the particle simulations began in a time-reversed sense. STILT was configured to simulate the paths of 1000 particles backwards

in time 6 hours at each receptor.

3.2.2.2 *Footprint*. Back trajectories are used to identify upwind areas that influence concentration measurements at each STILT receptor. The location and duration of STILT particle simulations along their paths to reach the STILT receptor time and location are compiled into a sensitivity that is known as a "footprint". The footprint sensitivity, $f(\mathbf{x}_r, t_r | x_i, y_j, t_m)$, henceforth F, can be described as the impact on concentration at the STILT receptor due to the upwind surface influence, where $\mathbf{x}_r$ represents the location of the air parcel at time, t_m. It also represents the surface influence on an air parcel arriving at the receptor location based on the duration of each particle in upwind locations as the sum over all parcels (p=1, N_{tot}) at x_i, y_j, over the depth of the PBL (h) with a density (ρ) for each time step $\Delta t_{p,i,j,k}$. Mathematically, this quantity can be expressed as:

$$f(\boldsymbol{x}_r, t_r | x_i, y_j, t_m) = \frac{m_{air}}{h\rho(x_i, y_j, t_m)} \frac{1}{N_{tot}} \sum_{p=1}^{N_{tot}} \Delta t_{p,i,j,k} \quad (1)$$

STILT footprints (LHS) can be simulated in both forecast and analysis modes. In forecast mode, footprints identify the upwind regions that are mostly likely to contribute to observed downwind concentration enhancements. When used in analysis mode, footprints are used to explain observed enhancements (ΔCH_4; [2]) at each STILT receptor location. The upwind areas can also be matched to emission grids to determine the accuracy of existing emission estimates, or alternatively matched to concentration measurements ($CH_{4\ downwind}$, $CH_{4\ upwind}$; downwind and upwind methane concentrations, respectively) to produce an independent flux estimate (Φ_{CH4}).

$$\Delta CH_4 = CH_{4\ downwind} - CH_{4\ upwind} \quad (2)$$

$$\Phi_{CH4} = \frac{\Delta CH_4}{F} \quad (3)$$

In forecast mode, STILT receptors can be defined based on areas over which the fluxes are to be estimated. The time and placement of both STILT receptors and footprints must exist within the spatiotemporal domain of the driving meteorological forecast grid. Because the footprint represents the upwind areas, this means the start of the footprint (in a time-forward sense) cannot occur before the forecast analysis time, and the forecasted time of the receptor observation cannot exceed the last forecast validation time contained in the driving meteorological forecast grid.

3.2.3 Flight planning

The goal of creating time-reversed forecasts was to design flight patterns that characterize changes in methane concentration as air is tracked from originating locations to arrival at each target location. To achieve this goal, time-reversed STILT forecasts were initialized for times that corresponded to midway through each flight and the end of each flight. Forecasts were interpolated in time as needed based on the forecast hours available. Plots of STILT particle locations showed the spatial extent and direction of where the air arriving at each receptor originated during the first half of each flight. This allowed for flexibility in the order in which targets were sampled, the possibility to sample targets and upwind locations at multiple times, and the addition of targets of opportunity related to other mission goals.

To aid in the collection of aircraft observations that promote the estimation of emissions using a Lagrangian model, real-time STILT forecasts were created each day during the Carbon in Arctic Reservoirs Experiment in California (CARVE-CA) field campaign that took place in the San Joaquin Valley during 21-24 April 2014. Although

the results will not be shown in this current study, the models and implementation are relevant to the implementation of LEAF. The time-reversed forecasts were based on the Global Forecasting System (GFS), the North American Mesoscale (NAM) model, and the Rapid Refresh (RAP) model with 1000 4-hour duration particle back-trajectories centered at the middle and end of the flights. The forecasts each had a spatial resolution of 28 km, 12 km, and 3 km respectively with respective temporal resolutions of 3, 3, and 1 hour for the same-day forecasts made each morning at the time of the forecasts. STILT was configured to update every 6 hours based on the most recent forecast from each model to determine from where the air arriving at targets of interest originates (i.e., the upwind).

3.2.4 Measurements

This study uses aircraft-based measurements from two different aircraft over two different regions of the U.S. to demonstrate the broad applicability of these methods. Surface wind measurements were also used to ensure the quality of the model analyses. The aircraft and surface-based wind measurements used in each area are described.

3.2.4.1 *Uinta Basin Ozone study*. The goal of the Uinta Basin Ozone study was to determine the processes that contribute to the wintertime ozone production. In conjunction with the atmospheric chemistry observations, NOAA carried out airborne observations of greenhouse gases (Karion et al. 2015). More about the experiment is described therein. For this experiment used the NOAA flight planning tool.

The first set of measurements described in this paper was collected 3-20 February 2012 and 31 January – 7 February 2013 in the Uinta basin of Utah. The Uinta Basin is an enclosed mountain basin in the northeast corner of Utah. The Uinta Basin is a place with

much oil and natural gas development. A single-engine turboprop aircraft flew 12 flights in 2012 and 6 in 2013. These flights typically lasted about 3 hours. The measurements of primary use in this study were collected from a continuous cavity ringdown spectroscopy (CRDS) instrument that measured methane, carbon dioxide, carbon monoxide, and water vapor analyzer with a sampling frequency of 10 s in 2012 and 5 s in 2013.

3.2.4.2 *Wind measurements*. Wind observations were used to assess the quality of the meteorological analyses that drive the LPDM and to estimate the uncertainties associated with imperfect wind analyses. Wind measurements in this study were made using the High-Resolution Doppler Lidar (HRDL) and Mesowest in the Uinta Basin. Further details about HRDL and Mesowest are available from Grund et al. (2001) and Horel et al. (2002), respectively.

For this study, the HRDL winds are used to corroborate the height of the PBL height estimated from aircraft-measured trace gas concentrations (methane, water vapor, carbon dioxide, and carbon monoxide when available). Both Mesowest and HRDL winds were used to assess the quality of meteorological analyses used in STILT and to characterize wind errors.

3.2.5 STILT receptor definition and placement

Emissions estimated using an LPDM necessitate careful definition and characterization of the “receptors”. Receptors are locations from which STILT particles are initialized and propagated backwards in time. Not only is the receptor the starting point for time-inverted simulations of particle movement but the characterization of methane concentrations at the receptor comprises the first part of (2). Therefore, one must

select the spatial scales that must describe the emission sources of interest and differentiate areas of elevated methane that arise from emission sources from ambient (background) values. Methane concentrations associated with each receptor have importance equal to the upwind concentration in the calculation. The definition of the receptor is the part of the equation that characterizes the area between the features of interest, and the corresponding downwind (receptor) concentration (2). The receptor definition then also provides opportunities to improve upon each of these aspects.

This study investigated multiple ways to define STILT receptors. The following assumptions and quality assessments were used to determine the most suitable methods:

1. Methane emissions are detectable as observed, elevated methane concentrations at the receptor, as compared to corresponding upwind concentrations;
2. Methane emissions originate from point-based or area-based surface sources that are expressed as consecutive observations of elevated methane concentrations, relative to nearby areas;
3. Point-based or area-based emission sources may be expressed together or separately over an area;
4. If possible, minimize uncertainty that arises from the representation of methane concentrations at the receptor.
5. The method can be broadly applied to a large number of aircraft flights.

These definitions and criteria provided some of the motivation for the methods explored to estimate fluxes. We explored a variety of receptor definitions based on methods and parameters used in other studies then compared against the 3 February 2012 case in Karion et al. (2013), henceforth referred to as K2013. Among the receptor definitions

tested were:

1. consecutive values in excess of a fixed quantile of methane concentration;
2. a regularized 5-minute mean; and,
3. time series-based features that fall under the broad umbrella of change point methods.

We will focus on the third. Methods to define STILT receptors increase in complexity from methods 1) to 3) within the list above. This study will focus on the change point method, which was the final adopted method.

3.2.5.1 *Change point*. Change point methods were used to identify STILT receptors. The most important advantage in the use of change point methods is the ability to create segments of consecutive observations that are likely to have occurred from the same distribution with the same mean and variance. It is also an advantage that each segment demonstrates statistical properties (a mean and variance) that differ from adjacent segments. The mean is needed for the enhancement calculation (2), and the variance needed to estimate the uncertainty due to the representativeness of the concentrations at the receptor.

Broadly, change point methods detect the location in a time series where a statistic changes significantly from the observations occurring before it and after it (referred to as “segments”). In this study, change point methods are applied to methane concentrations to detect changes in mean and variance (Fig. 3.2). These statistics were selected to separate segments in which methane enhancements are detected from areas that are more representative of ambient background concentrations or other features (i.e., the free troposphere portion of a flight).

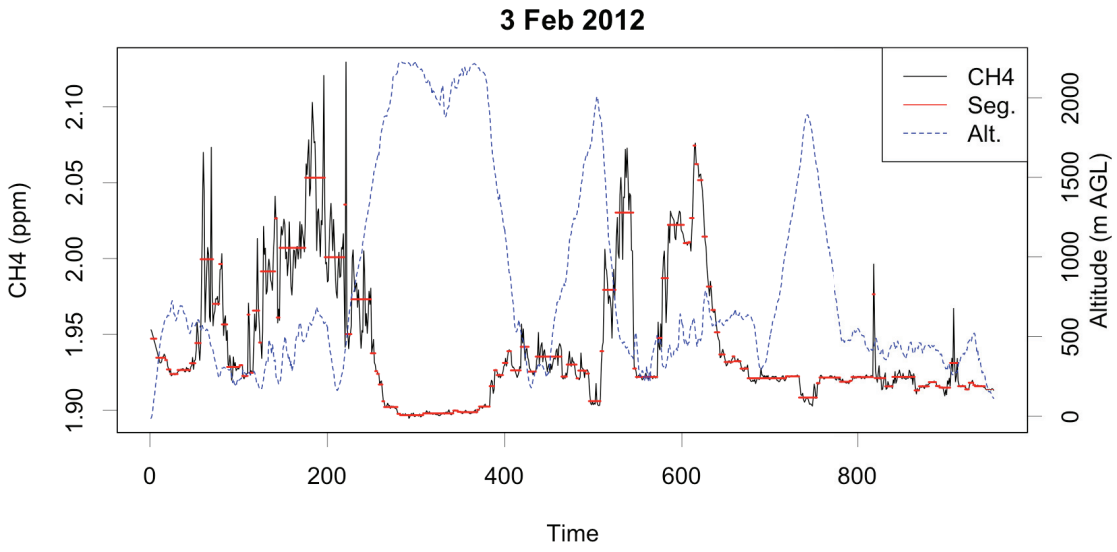

Figure 3.2: The PELT change point method segments (red) are determined from a time series of methane concentrations (ppm) that have similar mean and variance. Aircraft altitude is also shown (blue dashed line). X-axis shows seconds from beginning of the 3 February 2012 flight over the Uinta Basin.

To apply a change point method, measurements are grouped together sequentially to populate a distribution. The selected statistic is calculated for that distribution. The next sequential observation is then tested to determine if it is likely to lie within the distribution populated by the observations before it. The groupings of observations before and after the change point comprise segments, each of which have the possibility to define a LPDM receptor, contain observations that can be described by a distribution that expresses the selected statistic (e.g., observations that fall within a normal distribution around the mean). Most often, change point algorithms minimize a cost function and apply a penalty (e.g., the Akaike Information Criterion) that decreases as the quality of fit improves (alternatively, in direct relation to the "badness" of fit). Usually, there is an assumption or specification of distribution type over which the selected statistic is computed.

Multiple change point methods result from the recursive application of the change point algorithm to all segments detected prior to its most recent application. When change points are detected in mean and variance, it ensures each receptor value (based on the mean concentration of the segment) and associated representativeness uncertainty (based on segment variance) are well characterized. The use of change point does not result necessarily in a decrease in receptor-level uncertainty. It means instead that the mean and variance along each segment differ from nearby measurements.

Pruned Exact Linear in Time (PELT; Killick and Eckley (2014)) is a method that minimizes a cost function while excluding observations in the time series that cannot be the minima (pruning). It is an exact search method, which means the algorithm uses a set of equations to produce an optimal solution (cf. approximation methods). The number of

segments detected increases linearly with the length of the time series. Change points are distributed throughout the time series. The PELT method prevents the possibility of all detected change points lying within a single portion of the time series.

Figure 3.2 shows the measured values of methane concentration and altitude with the mean of methane-based change point segments determined using the PELT method during the 3 February 2012 case. The PELT method was able to group together portion of the time series with low mean and low variance in methane concentrations. These indicate when the aircraft was above the PBL. Likewise, the areas in which the mean and variance were large are also indicated and grouped together in a segment.

Of the variety of change point methods to define receptors, the PELT change point method resulted in the identification of cohesive features. This method resulted in the receptor locations shown in Fig. 3.3. PELT is broadly applicable with less modification, and results in the largest number of positive emission values.

3.2.6 Assessment of analyses

To characterize upwind locations and concentrations, STILT relies on meteorological analyses to produce time-varying winds. Other relevant parameters are also used in the STILT runs. These STILT runs are used to identify likely areas from which air arrives at the STILT receptor. For the field campaigns described here, the NAM provided the relevant meteorological analyses. Based on the selection of the NAM for the driving meteorological analyses, HRDL winds and Mesowest surface winds were used to select cases in which the NAM showed boundary layer winds were consistent in speed and direction with the observed. These criteria lead to the inclusion of 10 out of the 20

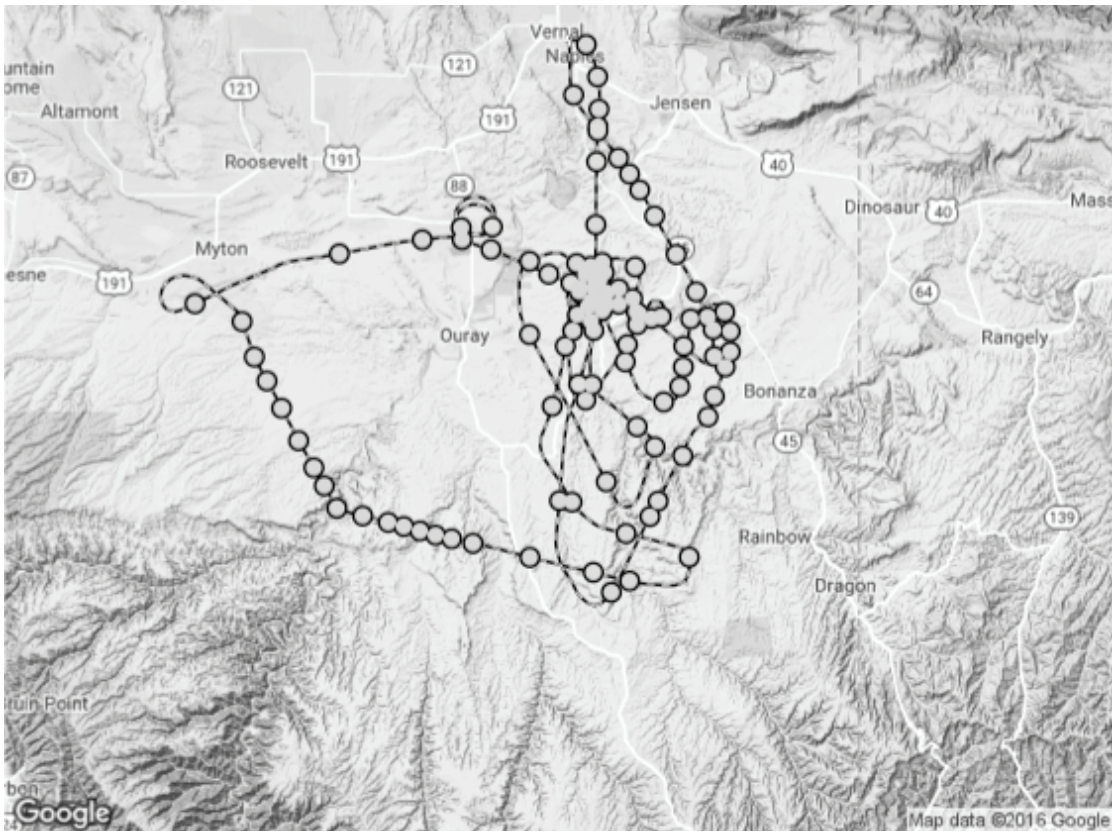

Figure 3.3: Map showing the spatial locations of change point-based receptors (gray dots) along the aircraft flight track (dashed line) for 3 February 2012.

flights for the Uinta Basin.

3.2.7 STILT simulations

Initial STILT simulations were created at receptor locations and run backwards in time for 6 hours. PBL heights were validated based on the detection of rapid changes in the above ground wind and concentration measurements. A second set of runs was made in which the PBL heights from the NAM were scaled according to observations.

Errors in the wind analysis affect the quality of the STILT footprints produced. Wind error statistics derived from Mesowest and HRDL were used in the second set of runs to simulate the effects of wind errors in the analyses from a third set of runs ("transport error"; Lin and Gerbig (2005)). The transport error parameters for 3 February 2012 had standard deviations of 1.9 m s^{-1} for wind errors, a horizontal error correlation length scale of 105 km, an error correlation time scale of 60 min, and a vertical error correlation of 1 km.

3.2.8 Estimation of methane fluxes and associated uncertainties

Both the upwind and downwind parts of (2) are needed to produce a fugitive emission rate. STILT receptors define the downwind values. Upwind values are based on the STILT footprint.

As the model propagates particles backwards in time during each run, LEAF matches modelled upwind particle locations to measured upwind portions of each aircraft flight. These particles are matched to the nearest upwind aircraft observation collected prior to the STILT receptor definition from which the particles are initialized. Methane

concentrations are then assigned to each particle based on the nearest upwind aircraft measurement for both the STILT runs with the PBL height scaling and for the STILT transport error runs. Figure 3.4 provides an overview schematic of the matching order relative to aircraft measurement collection.

In addition to the distance-minimization, the matching between particles and upwind aircraft measurements must be more than 4 km from the receptor and in a different change point segment from the receptor to ensure the receptor and upwind particle-observation match are from different features. This technique is applied to estimate both the methane flux and the uncertainty incurred from an imperfect wind analysis (transport error).

3.2.8.1 *Methane flux quantification*. Estimates are based on the characteristics of observed differences in concentration measurements between upwind locations (i.e., time-reversed particle locations) and at STILT receptors. These differences are weighted according to the strength of footprint to surface influence based on the length of time and probable locations of air parcels originating from upwind regions within the planetary boundary layer.

To estimate methane emissions, the enhancement between the downwind/upwind (2) is normalized according to the sum of the footprint sensitivity to produce a flux estimate (in units of μmol m^{-2} s^{-1}) (3). These estimates assume a constant emission rate for the duration of the footprint. A composite of all footprints from the 3 February 2012 case is shown in Fig. 3.5.

The use of STILT is advantageous because it is an LPDM that can characterize the upwind portion of the methane enhancement. The downwind portion is equally

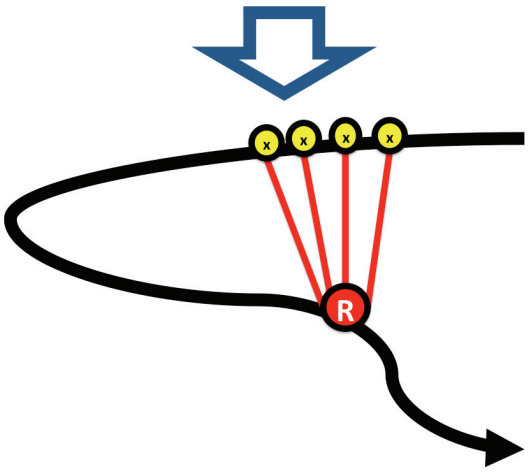

Figure 3.4: Matches between the time-inverted particles on their trajectories (solid red) that originate from the STILT receptor (R) are shown. Upwind aircraft measurements (x) are matched to particle simulations based on the shortest distance.

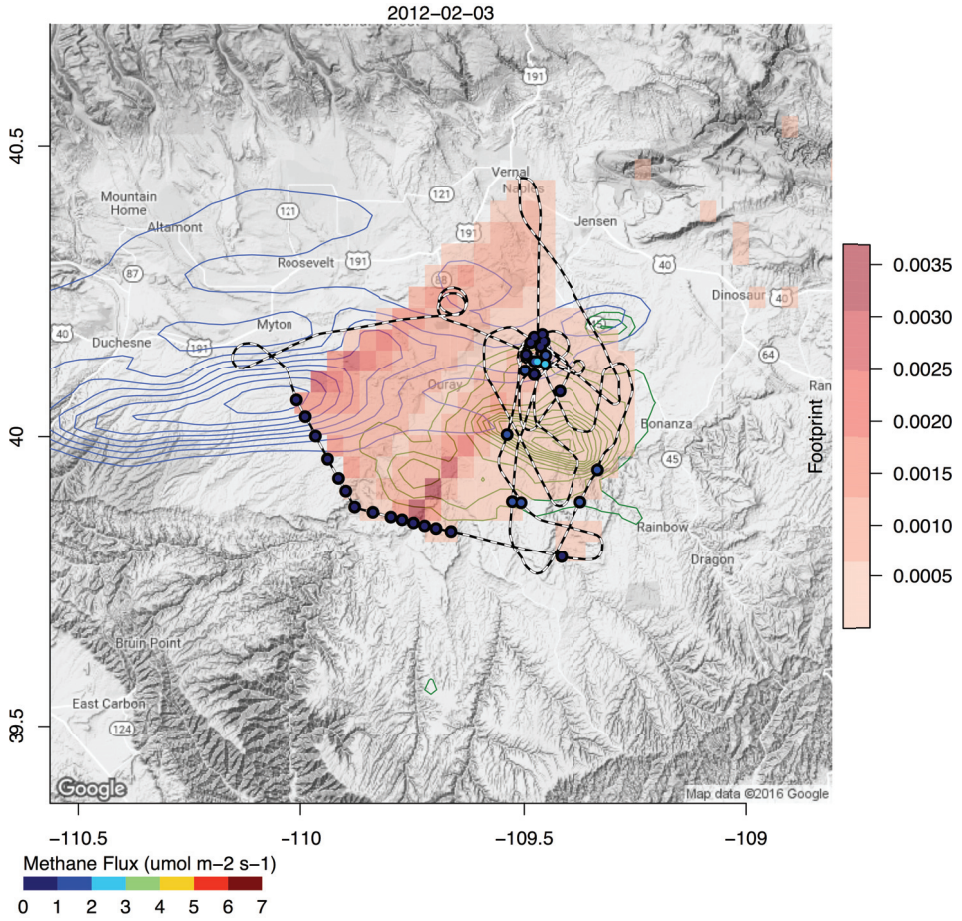

Figure 3.5: A composite image of STILT footprints for 3 February 2012 is shown with LEAF-estimated methane fluxes (μmol m^{-2} s^{-1}). Oil well locations (dark blue contours) and gas well locations (dark green contours) are shown for Uintah and Duchesne counties.

important and is influenced the most easily through user decision. The use of PELT increases the robustness of an upwind definition based on grouping together portions of the flight that have similar mean and variance, which is also advantageous for uncertainties in the flux estimate. Both the upwind and downwind have associated uncertainties that add to the uncertainty of the methane flux estimate as a whole.

3.2.8.2 *Uncertainty estimation*. The uncertainty associated with each receptor was based on the total variance of: the uncertainty due to the representativeness of the change point segment at which the receptor was defined ([4], representativeness), the uncertainty due to an imperfect wind analysis ([5], transport error), the quality of upwind sampling (missed upwind), and 10% of the STILT footprint (F_R).

$$\sigma_{Rep}^2 = \frac{\sigma_{seg}^2}{dF} \tag{4}$$

$$\sigma_{Transport}^2 = \sigma_{CH4up,trans}^2 - \sigma_{CH4up}^2 \tag{5}$$

$$\sigma_{tot} = \frac{\sqrt[2]{\sigma_{Transport}^2 + \sigma_{Rep}^2 + \sigma_{Missed}^2}}{(1 \pm 0.1) * F_R} \tag{6}$$

The variance of methane concentrations along each change point segment was used to estimate the representativeness error. The degrees of freedom were adjusted according to the autocorrelation of methane concentrations along the segment. The transport error derived from another run of the STILT model, in which uncertainties in the wind field were propagated directly in the motion of the STILT particles (Lin and Gerbig, 2005), following a distribution characterized by error statistics. These error statistics that describe the errors in the zonal and meridional wind were used as parameters in the transport error run had a standard deviation of 1.9 m s^{-1}, 105 km

horizontal error correlation length scale, 60 minute time scale error correlation, and a vertical error correlation of 1 km. To account for the uncertainty in imperfect sampling of the upwind (as indicated by the separation between the particle and the upwind aircraft location), a spatial statistical technique was adopted (Kitanidis 1997). Semivariograms were constructed to describe the relationship between the variance of the difference between methane values, as a function of the distance between each particle and nearest upwind aircraft measurement match. Separate semivariograms were used for distances within the PBL and within the free atmosphere (Fig. 3.6).

Each of the three sources of uncertainty is estimated for every receptor. Figure 3.7 shows the relative contributions of each source of uncertainty to the total uncertainty for each case. The dominant term is the uncertainty due to the transport error. It averages 82% of the error for all cases, followed by the missed upwind (10%) and representativeness error (7%). This largely reflects the quality of the NAM analysis, which was of high quality for 3 February 2012. The size of the terms is also affected by receptors that had a distance between particle and upwind match of > 4km (the grid resolution), which were discarded as poor matches. This limits the size of the uncertainty due to missed upwind observations.

3.2.8.3 *Area-wide estimates*. LEAF is used to create a basin-scale emission rate and to link other quantities that are best described on a larger scale (e.g., basin-specific gas production rates). After receptor-level methane flux and uncertainty estimates were made, each receptor was weighted (w_i) to produce a basin-wide flux estimate. Each receptor-level flux was weighted according to the total footprint (F_R) and inverse of the total uncertainty (σ_{Tot}) for each receptor, R (7).

(a)

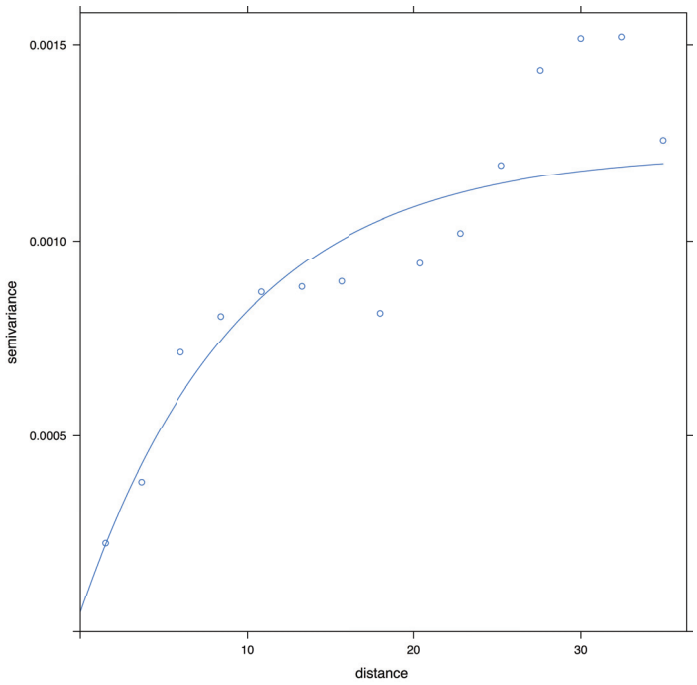

(b)

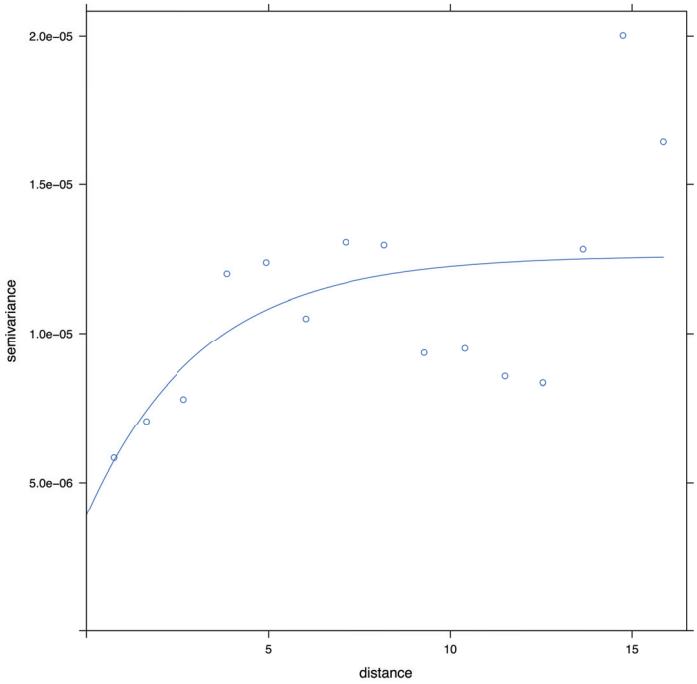

Figure 3.6: Semivariogram for methane within the Uinta Basin for 3 February 2012 (a) within the PBL and (b) above the PBL. The length scale is 35 km and 12 km, respectively.

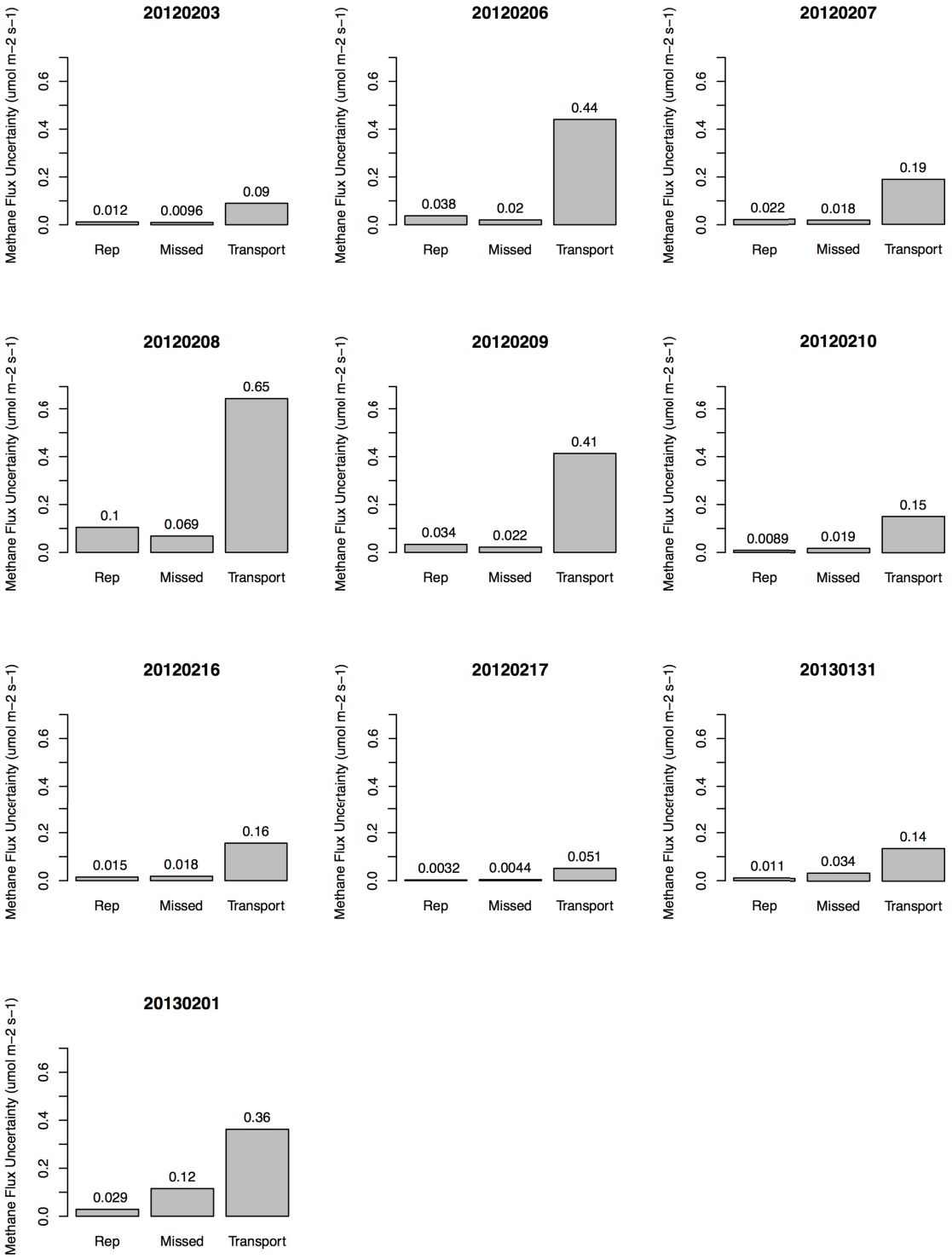

Figure 3.7: Relative sizes of uncertainty terms for 2012-2013 Uinta Basin flights. “Rep” is the uncertainty due to representativeness error. “Missed” is the uncertainty due to a mismatch between the aircraft location and upwind particle locations. “Transport” shows the uncertainty due to transport error.

$$w_i = \frac{\frac{F_R}{\sigma^2_{Tot,R}}}{\sum_{R=1}^{n_R} \frac{F_R}{\sigma^2_{Tot,R}}} \quad (7)$$

The same weights that were calculated for the flux assigned to each receptor were applied to the total uncertainty associated with each flux to create a basin-wide estimate.

3.3 **Results and Discussion**

Although we focused initially on the 3 February 2012 case, the same methods were applied to nine other cases during the 2012-2013 field campaigns. Flights covered different areas of the Uinta Basin, and areas of differing gas production rates (Fig. 3.8). Differences in the areas of gas production sampled during each flight contributed to differences in the fluxes estimated from each individual flight. Both the flux estimates and impact of coverage areas are discussed.

3.3.1 Uinta Basin

Fugitive emission rate estimates depend upon the number and spatial density of producing wells over the area. Figure 3.9 shows methane flux estimates for each flight as a function of oil and gas well density (number of wells per 16 km^2 grid spacing). Each flight covers a different area of the basin and contributes to variation in each methane flux estimate. There is a strong correlation between the number of wells within the STILT footprint and the methane fluxes estimated for each case. The largest methane flux uncertainty is during the 8 February 2012 case. The contribution from transport error was considerably larger than in other cases. This means the quality of the NAM analysis was the poorest of all cases used in this study (Fig. 3.7). This case also had the largest

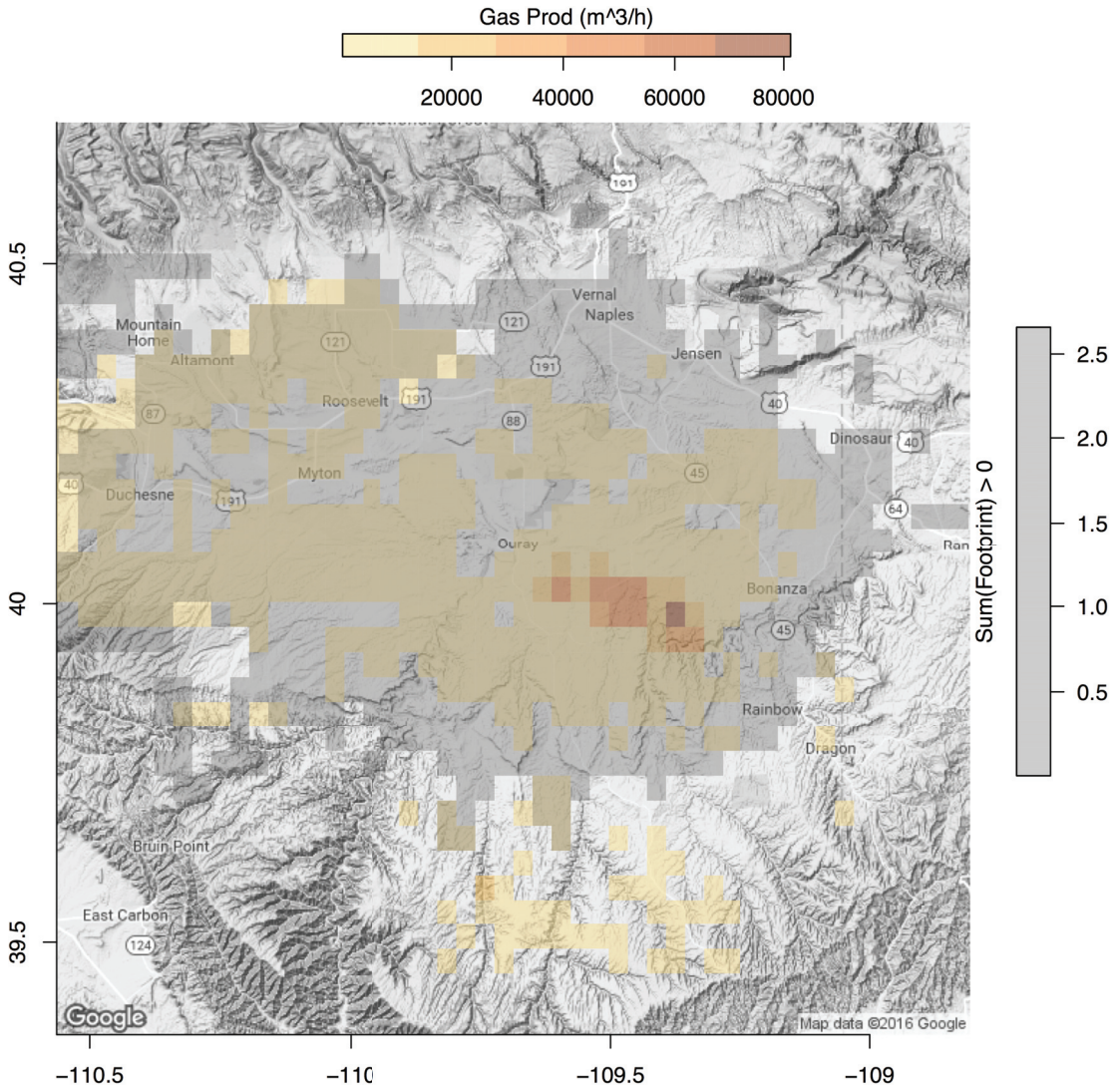

Figure 3.8: Hourly gas production at 4 km^2 resolution (m^3 h^{-1}) were created for Uintah and Duchesne counties based on reports from the Utah Department of Natural Resources. The gray areas indicate areas of footprint influence for any flight.

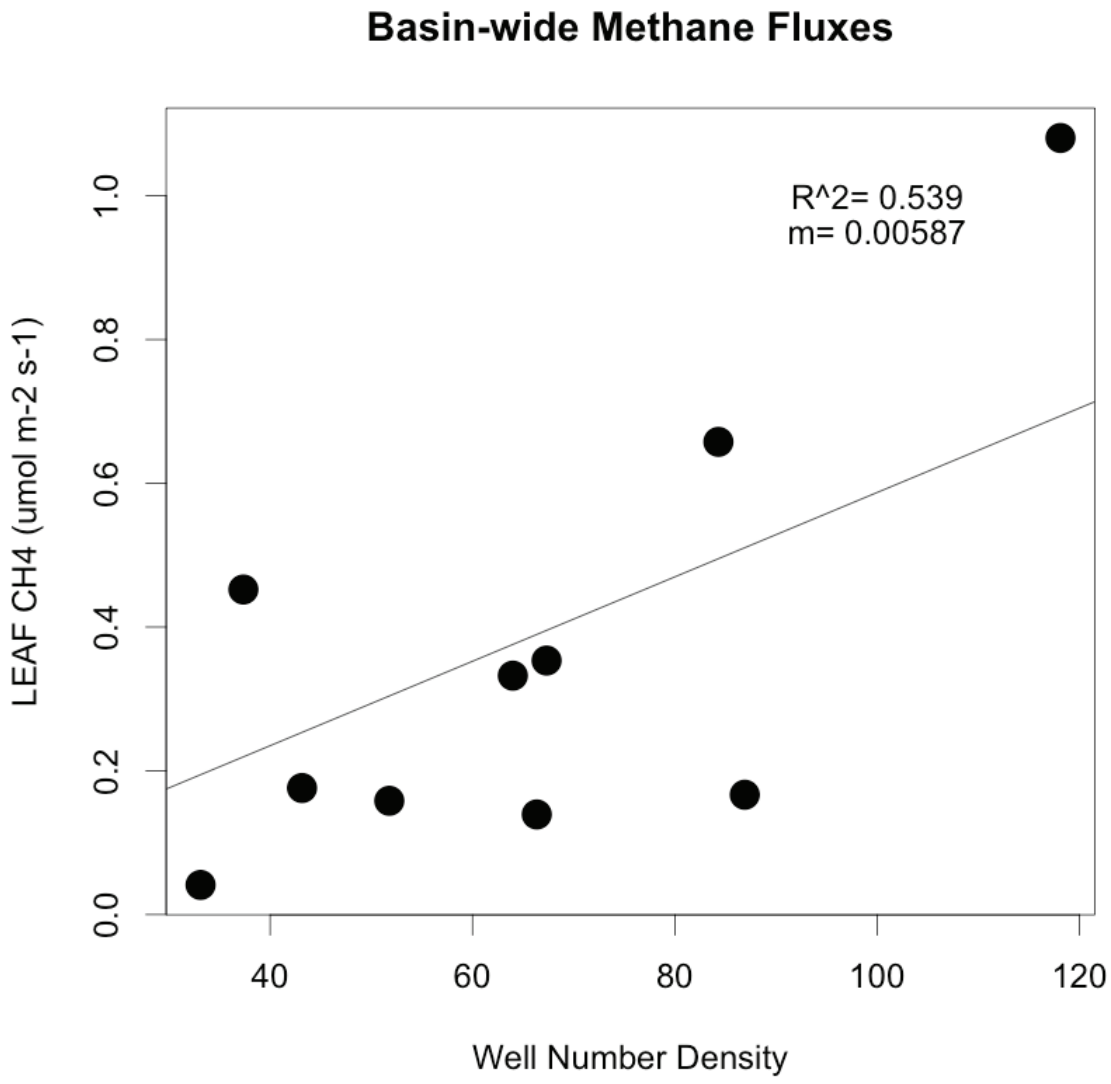

Figure 3.9: LEAF-estimated methane flux and well number density (number of wells per 4 km spacing) relationship is shown. The presence of any well (oil or gas) explains 0.539 of the variance in estimated methane fluxes.

uncertainty due to representativeness error at the receptor, which was an order of magnitude larger than any other case. This indicates improvements to the change point receptor definition and a better analysis could substantially decrease the total uncertainty.

One of the goals was to use LEAF to compare to existing estimates of fugitive emission rates in the Uinta Basin, such as the 3 February 2012 case presented in K2013. When the effects of areal coverage on the methane flux estimates are included, the LEAF estimate approaches the K2013 estimate. When using the same 2000 km^2 area to estimate the percentage of fugitive emissions from natural gas production, we find an emission rate of 39.4 t CH_4 h^{-1} (40.8 t CH_4 h^{-1}, less the 1.4 ± 1.1 t CH_4 h^{-1} from cattle and natural gas seeps that K2013 estimate), which is lower than the 54.6 t CH_4 h^{-1} estimated by K2013. When the total uncertainty from the LEAF estimates is included, this results in a fugitive methane emission rate of 39.4 ± 10.8 t CH_4 h^{-1}, or 8.2-4.7% of production, which approaches the 8.9% estimate from K2013. However, this estimate does not yet include the uncertainty of the production estimate itself, as estimated by K2013. When the production number uncertainty is included, this yields an estimate of fugitive emissions of 1.9-10.9% (6.4 ± 4.5%) of production for 3 February 2012, which compares to the 6.2-11.7% (8.9 ± 2.7%) K2013 estimate.

To further refine our estimate of fugitive emission rates for 3 February 2012, we use LEAF to calculate the area sampled by the aircraft more precisely. The intersection of the composite STILT footprint and the gas production area shown in Fig. 3.5 and Fig. 3.8 covers an area of 3575 km^2, which is substantially larger than the 2000 km^2 previously considered. Likewise, the increased area contributes to the estimate of natural gas produced over the area (Fig. 3.8), which is used in the fugitive emission calculation.

To include the effects of the larger area and gas production covered by the STILT footprints, we estimated a spatially allocated hourly gas production rate. Well-specific production reports were merged with well location data for both Uintah and Duchesne Counties (available from the Utah Department of Natural Resources Division of Oil, Gas, and Mining). The production numbers reported for each well are used to create a daily production estimate for each well during its reporting period. The daily production numbers are summed over 4 km x 4km grid cells, and converted to an average hourly production rate per unit area (Fig. 3.8) to produce a 16 km^2 resolution grids of gas production for February 2012 and February 2013. The net effect on the 3 February 2012 case was to increase the coverage area and area-accumulated gas production estimate, based on the intersection of active production areas with composite STILT footprint coverage areas.

Using the more accurate area from the intersection of the STILT composite footprint with the spatially allocated hourly gas production, we arrive at a methane emission estimate of 35.5 ± 9.3 t CH_4 h^{-1}. When we include a gas production uncertainty estimate similar to K2013, we arrive at an emission rate of 9.3 ± 5.2% of production over the STILT footprint coverage area for 3 February 2012, which overlaps with the 8.9 ± 2.7% previously estimated. Both exhibit a central estimate much higher than the fugitive emission rates for the Bakken shale in North Dakota (6.3 ± 2.1%; Peischl et al. 2016) and the Denver-Julesburg area (6.2 ± 2.0%; Pétron et al. 2014).

When the LEAF method is applied to the other nine cases in the Uinta Basin, we initially notice case-by-case variations. There is no obvious physical reason for this variation. The methane fluxes estimated from aircraft flights in the Uinta Basin are

mostly greater than zero and vary greatly based on the molar fluxes (Fig. 3.10). The production rates of the areas sampled likely impact the methane molar fluxes calculated. When converting the molar flux estimates to a fugitive emission rate as a percentage of production, there is less variability to the central estimates for each case (Fig. 3.11). We also notice larger uncertainties are associated with each fugitive emission estimate. The LEAF derived uncertainty combined with the uncertainty associated with the gas production numbers cannot completely preclude fugitive emissions rates of less than 2%.

The uncertainties for most cases may be overestimated. When we look closer at the uncertainties calculated from each case, the central emission estimates usually fall within the uncertainty bounds of all other cases. Because the uncertainty is calculated at ± 1σ, then 68% of the other estimates should fall within the uncertainty bounds for each case, assuming a normal distribution. This is true for about seven of the ten cases (5-7 out of 9 fall within), so the uncertainty bounds are likely well calibrated under the assumptions made. The inclusion of unphysical (negative) fugitive emission rates that fall within the uncertainty bounds (except 3 February 2012 and 1 February 2013) is evidence some cases may have overestimated uncertainty, or that the uncertainties may be better estimated by nonparametric methods.

3.4 **Summary**

In this study, we refined a method, which we call "Lagrangian Estimation of Aircraft-derived Fluxes (LEAF)", to estimate methane emissions using aircraft measurements and a LPDM. We compared several ways to define LPDM receptors through the use of the change point analysis to define groups of consecutive aircraft observations with similar mean and variance. We then compared fugitive emission

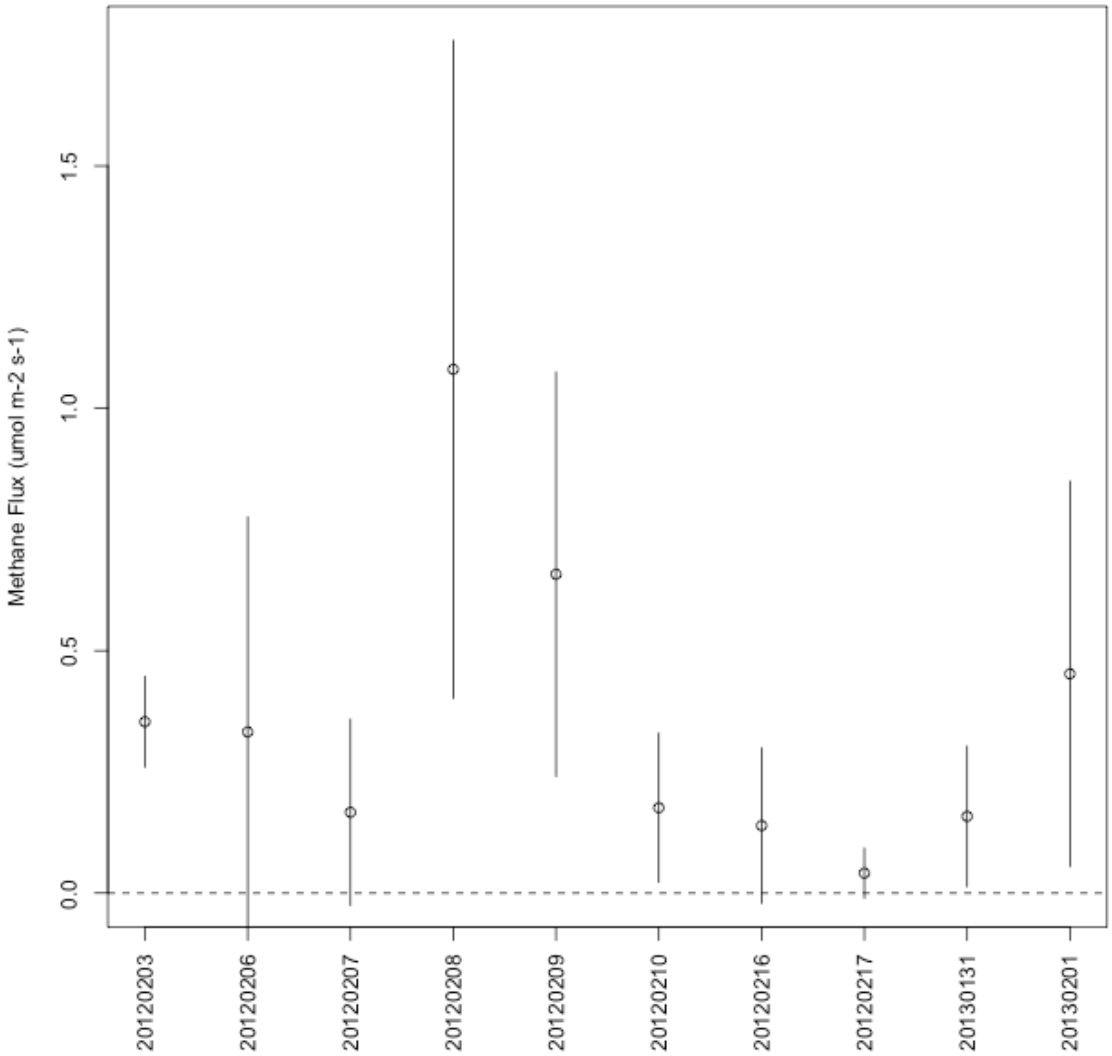

Figure 3.10: The daily variability of basin-wide fluxes is shown for each date.

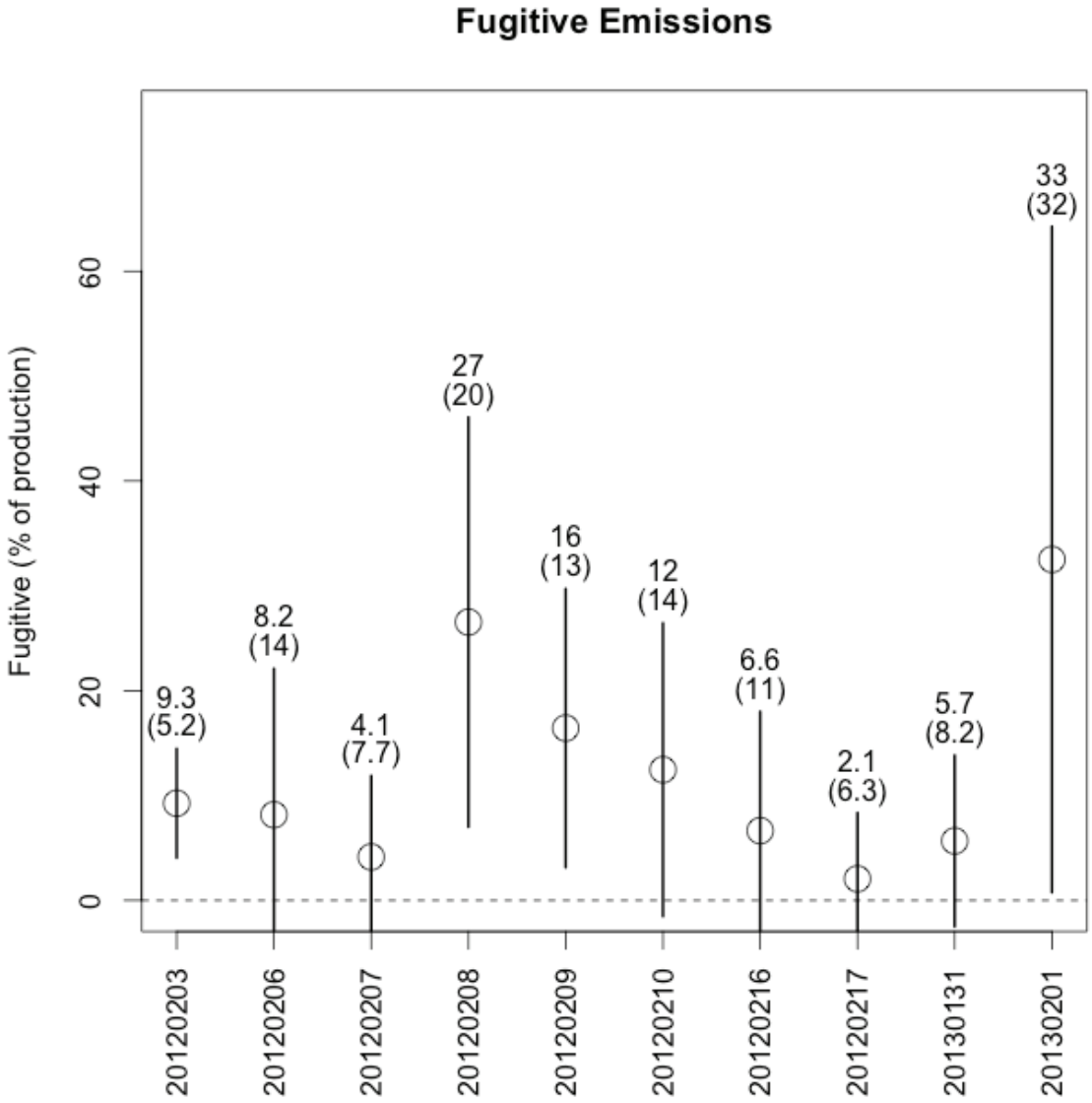

Figure 3.11: Fugitive emissions from LEAF, as a percentage of natural gas production. The uncertainty is shown in parentheses.

estimates to a box model-based estimate for 3 February 2012 to arrive at a fugitive emission rate of 9.3 ± 5.2%.

We estimate uncertainties associated with the quality of the driving meteorological model, the mismatch between the aircraft measurement and upwind location, the representativeness of the methane concentration at the receptor, and the natural gas production estimate. The largest contributor to uncertainty is transport error (it was the largest term in 60% of the cases), followed by uncertainty in the natural gas production estimate (largest in 40% of the cases). These sources of uncertainty could be addressed through the use of a higher quality meteorological analysis and a spatially allocated gas production grid that represents both spatial and temporal (seasonal) variations. For many cases, the uncertainty is likely to be overestimated.

When we combine sources of uncertainty and compare our fugitive emission rates to those of other studies, we find the Uinta Basin to have a fugitive emission rate similar to that of the Bakken shale (Peischl et al. 2016) and the Denver-Julesburg area (Pétron et al. 2014).

We were unable to exclude entirely the possibility of fugitive emission rates of less than 2%, but we included uncertainty from a variety of sources that is likely overestimated. Under the ideal conditions observed on 3 February 2012, we estimate the fugitive emission rate at 9.3 ± 5.2% of production. This number is about 20% more than the GAO/WRAP bottom-up estimate (5.07%) and 50% less than the 8.9% estimated by K2013. Each of these estimates provides evidence that the fugitive emission rates in the Uinta Basin likely exceed the limit needed to achieve a climatic benefit to natural gas over coal.

CHAPTER 4

CONCLUSION

Both PBL growth and techniques to estimate methane emissions improve our ability to constrain GHG emissions. Of primary importance to this work is methane, but the estimation of other GHGs such as carbon dioxide are easily applicable as well.

From the examination of PBL growth, two primary drivers of growth were found as skillful forecasts that could be made with a limited number of parameters. With only a limited number of parameters from a prior rawinsonde to initialize MASH and SHOT, each shows potential as a stand-alone PBL height forecast tool that requires hourly surface heat fluxes and friction velocity.

The PBL height was used as a scaling factor to estimate methane emissions derived from aircraft measurements. Time series analysis techniques along with improvements to the quantification of associated uncertainties lead to estimates of methane emissions in the Uinta Basin that validated existing estimates, thus demonstrating the applicability of the LEAF method for a broad range of analyses difficult to perform with other estimation methods.

Mitigating fugitive methane emissions is an effective opportunity to decrease an important short-term climate forcer that has the potential to mitigate the effects of longer term climate forcers, such as carbon dioxide. Decreasing fugitive methane emissions can be a net positive for climate, health, and industry. More work is needed to achieve further

accuracy needed to monitor and to detect fugitive emissions in way that will lead to cost-effective infrastructure improvements.

REFERENCES

Alvarez, R., S. Pacala, J. Winebrake, W. Chameides, and S. Hamburg, 2012: Greater focus needed on methane leakage from natural gas infrastructure. *PNAS*, **109,** 6435-6440.

Ball, F. K., 1960: Control of inversion height by surface heating. *Quarterly Journal of the Royal Meteorological Society*, **86,** 483-494.

Barr, A. G., and A. K. Betts, 1997: Radiosonde boundary layer budgets above a boreal forest. *Journal of Geophysical Research*, **102,** 29205-29212.

Batchvarova, E., and S. E. Gryning, 1991: Applied model for the growth of the daytime mixed layer. *Boundary-Layer Meteorology*, **56,** 261-274.

Boers, R., E. W. Eloranta, and R. L. Coulter, 1984: Lidar observatons of mixed layer dynamics: Tests of parameterized entrainment models of mixed layer growth rate. *Journal of Climate and Applied Meteorology*, **23,** 247-266.

Carson, D. J., 1973: The development of a dry inversion-capped convectively unstable boundary layer. *Quarterly Journal of the Royal Meteorological Society*, **99,** 450-467.

Deardorff, J. W., 1972: Parameterization of the planetary boundary layer for use in general circulation models. *Monthly Weather Review*, **100,** 93-106.

Dee, D. P., and Coauthors, 2011: The ERA-Interim reanalysis: Configuration and performance of the data assimilation system. *Quarterly Journal of the Royal Meteorological Society*, **137,** 553-597.

Denning, A. S., I. Y. Fung, and D. A. Randall, 1995: Latitudinal gadient of atmospheric CO2 due to seasonal exchange with land biota. *Nature*, **376,** 240-243.

Denning, A. S., D. A. Randall, G. J. Collatz, and J. Piers, 1996: Simulations of terrestrial carbon metabolism and atmospheric CO2 in a general circulation model. Part 2: Simulated CO2 concentrations. *Tellus*, **48B,** 543-567.

Delisle, G., 2007: Near-surface permafrost degradation: How severe during the 21st century? *Geophysical Research Letters*, **34**.

Desai, A. R., K. J. Davis, C. J. Senff, S. Ismail, E. V. Browell, D. R. Stauffer, and B. P. Reen, 2005: A case study on the effects of heterogeneous soil moisture on mesoscale boundary-layer structure in the southern Great Plains, U.S.A. Part I: Simple Prognostic Model. *Boundary-Layer Meteorology*, **119,** 195-238.

Durre, I., R. S. Vose, and D. B. Wuertz, 2006: Overview of the integrated global radiosonde archive. *Journal of Climate*, **19,** 53-68.

Energy, G., 2010: Western Wind and Solar Integration Study. *The National Renewable Energy Laboratory*, Denver, CO.

Garratt, J. R., 1993: Sensitivity of climate simulations to land-surface and atmospheric boundary-layer treatments – a review. *Journal of Climate*, **6,** 419-448.

Garrett, A. J., 1982: A parameter study of interactions between convective clouds, the convective boundary layer, and a forested surface. *Monthly Weather Review*, **110,** 1041-1059.

Gentner, D. R., and Coauthors, 2014: Emissions of organic carbon and methane from petroleum and dairy operations in California's San Joaquin Valley. *Atmospheric Chemistry and Physics*, **14,** 4955-4978.

Gerbig, C., S. Korner, and J. C. Lin, 2008: Vertical mixing in atmospheric tracer transport models: Error characterization and propagation. *Atmospheric Chemistry and Physics*, **8,** 591-602.

Gerbig, C., A. J. Dolman, and M. Heimann, 2009: On observational and modelling strategies targeted at regional carbon exchange over continents. *Biogeosciences*, **6,** 1949-1959.

Grund, C., R. Banta, J. George, J. Howell, M. Post, R. Richter, and A. Weickmann, 2001: High-resolution doppler lidar for boundary layer and cloud research. *Journal of Atmospheric and Oceanic Technology*, **18,** 376-393.

Holzworth, G. C., 1967: Mixing depths, wind speeds and air pollution potential for selected locations in the United States. *Journal of Applied Meteorology*, **6,** 1039-1044.

Horel, J., and Coauthors, 2002: Mesowest: Cooperative Mesonets in the Western U.S. *Bulletin American Meteorological Society***, 83**, 211-225.

Karion, A., and Coauthors, 2013: Methane emissions estimate from airborne measurements over a western United States natural gas field. *Geophysical Research Letters*, **40,** 4393-4397.

Karion, A., and Coauthors, 2015: Aircraft-based estimate of total methane emissions from the Barnett Shale region. *Environmental Science & Technology*, **49,** 8124-8131.

Killick, R., and I. A. Eckley, 2014: Changepoint: An R package for changepoint analysis. *Journal of Statistical Software*, **58,** 1-19.

Kitanidis, P. K., 1997: *Introduction to Geostatistics: Applications in Hydrogeology.* Cambridge Univ. Press, Boston, MA.

Kretschmer, R., C. Gerbig, U. Karstens, and F. T. Koch, 2012: Error characterization of CO2 vertical mixing in the atmospheric transport model WRF-VPRM. *Atmospheric Chemistry and Physics*, **12,** 2441-2458.

Kretschmer, R., and Coauthors, 2014: Impact of optimized mixing heights on simulated regional atmospheric transport of CO2. *Atmospheric Chemistry and Physics*, **14**, 7149-7172.

Lilly, D. K., 1968: Models of cloud-topped mixed layers under a strong inversion. *Quarterly Journal of the Royal Meteorological Society*, **94,** 292-309.

Lin, J. C., and C. Gerbig, 2005: Accounting for the effect of transport errors on tracer inversions. *Geophysical Research Letters*, **32**, L01802.

Lin, J. C., and Coauthors, 2004: Measuring fluxes of trace gases at regional scales by Lagrangian observations: Application to the CO_2 Budget and Rectification Airborne (COBRA) study. *Journal of Geophysical Research*, **109**, D15304.

Lin, J. C., and Coauthors, 2006: What have we learned from intensive atmospheric sampling field programmes of CO2? *Tellus B*, **58,** 331-343.

Lyon, D. R., and Coauthors, 2015: Constructing a spatially resolved methane emission inventory for the Barnett Shale region. *Environmental Science & Technology*, **49,** 8147-8157.

McGrath-Spangler, E. L., and A. S. Denning, 2012: Estimates of North American summertime planetary boundary layer depths derived from space-borne lidar. *Journal of Geophysical Research*, **117**, D15.

Medeiros, B., A. Hall, and B. Stevens, 2005: What controls the mean depth of the PBL? *Journal of Climate*, **18,** 3157-3172.

Montzka, S. A., E. J. Dlugokencky, and J. H. Butler, 2011: Non-CO_2 greenhouse gases and climate change. *Nature*, **476,** 43-50.

Pielke, R. B., R. Avissar, M. Raupach, A. J. Dolman, X. Zeng, and A. S. Denning, 1998: Interactions between the atmosphere and terrestrial ecosystems: Influence on weather and climate. *Global Change Biology*, **4,** 461-475.

Peischl, J., and Coauthors, 2012: Airborne observations of methane emissions from rice cultivation in the Sacramento Valley of California. *Journal of Geophysical Research: Atmospheres*, **117,** D00V25.

Pétron, G., and Coauthors, 2014: A new look at methane and nonmethane hydrocarbon emissions from oil and natural gas operations in the Colorado Denver-Julesburg Basin. *Journal of Geophysical Research: Atmospheres***,** n/a-n/a.

Pielke, R. B., R. Avissar, M. Raupach, A. J. Dolman, X. Zeng, and A. S. Denning, 1998: Interactions between the atmosphere and terrestrial ecosystems: Influence on weather and climate. *Global Change Biology*, **4,** 461-475.

Rigby, M., and Coauthors, 2008: Renewed growth of atmospheric methane. *Geophysical Research Letters*, **35**, L22805-L22811.

Saha, S., and Coauthors, 2010: The NCEP Climate Forecast System Reanalysis. *Bulletin of the American Meteorological Society*, **91,** 1015-1057.

Saunois, M., and Coauthors, 2016: The Global Methane Budget: 2000-2012. *Earth System Science Data Discussions***,** 1-79.

Schaefer, H., and Coauthors, 2016: A 21st century shift from fossil-fuel to biogenic methane emissions indicated by 13CH4. *Science*, **352**, 80-84

Schwietzke, S., and Coauthors, 2016: Upward revision of global fossil fuel methane emissions based on isotope database. *Nature*, **538,** 88-91.

Seibert, P., F. Beyrich, S. E. Gryning, S. Joffre, A. Rasmussen, and P. Tercier, 2000: Review and intercomparison of operational methods for the determination of the mixing height. *Atmospheric Environment*, **34,** 1001-1027.

Seidel, D. J., Y. Zhang, A. Beljaars, J.-C. Golaz, A. R. Jacobson, and B. Medeiros, 2012: Climatology of the planetary boundary layer over the continental United States and Europe. *Journal of Geophysical Research: Atmospheres*, **117,** D17106.

Shindell, D. T., G. Faluvegi, D. M. Koch, G. A. Schmidt, N. Unger, and S. E. Bauer, 2009: Improved attribution of climate forcing to emissions. *Science*, **326,** 716-718.

Smith, E. A., and Coauthors, 1992: Area-averaged surface fluxes and their time-space variability over the FIFE experimental domain. *Journal of Geophysical Research*, **92,** 18599-18622.

Stocker, T. F., Q. Dahe, and G. Plattner, 2013: Climate Change 2013: Technical Summary.

Stull, R. B., 1976: Mixed-layer depth model based on turbulent energetics. *Journal of the Atmospheric Sciences*, **33,** 1268-1278.

Stull, R. B., 1988: *An Introduction to Boundary Layer Meteorology.* Kluwer Academic Publishers, 666 pp.

Taylor, K. E., 2001: Summarizing multiple aspects of model performance in a single diagram. *Journal of Geophysical Research*, **106,** 7183.

Tennekes, H., 1973: A model for the dynamics of the inversion above a convective boundary layer. *Journal of the Atmospheric Sciences*, **30,** 558-567.

Tennekes, H., and A. G. M. Driedonks, 1981: Basic entrainment equations for the atmospheric boundary layer. *Boundary-Layer Meteorology*, **20,** 515-531.

Turner, A. J., and Coauthors, 2016: A large increase in U.S. methane emissions over the past decade inferred from satellite data and surface observations. *Geophysical Research Letters*, **43,** 2218-2224.

von Engeln, A., and J. Teixeira, 2013: A planetary boundary layer height climatology derived from ECMWF reanalysis data. *Journal of Climate*, **17**, 6575-6590

Yan, H., and R. A. Anthes, 1988: The effect of variations in surface moisture on mesoscale circulations. *Monthly Weather Review*, **116,** 192-208.

Zhong, S., C. D. Whiteman, and X. Bian, 2004: Diurnal evolution of the three-dimensional wind and temperature structure in California's Central Valley. *Journal of Applied Meteorology*, **43,** 1679-1699.